UNIVERSIDADE DE SÃO PAULO

Instituto de Física de São Carlos

Ana Luiza R. F. Ferrari

Real-space formulation of the Numerical Renormalization Group method (NRG)

São Carlos

2022

Ana Luiza R. F. Ferrari

Real-space formulation of the Numerical Renormalization Group method (NRG)

Dissertation presented to the Graduate Program in Physics at the Instituto de Física de São Carlos, Universidade de São Paulo to obtain the degree of Master of Science.

Concentration area: Basic Physics

Advisor: Prof. Dr. Luiz Nunes de Oliveira

Corrected version

(Original version available on the Program Unit)

São Carlos

2022

This thesis was written concomitantly to my paper with Prof. Luiz Nunes de Oliveira *. They contain similar passages and the same figures. Chapter 2 also has elements in common with my MSc thesis at the University of Koeln, which is available online* †.

Acknowledgements

I would like to express my deepest gratitude to my advisor Luiz Nunes de Oliveira, for the patience and will to teach me the ways of research since my BSc. His kind supervision changed the career path of all his students, and I am no exception.

I wish to show my appreciation for my former desk neighbors, Luiz B. Guessi and Krissia Zawadzki. Their discussions and presentations sparked my interest and led me to take my first steps into NRG.

I am also grateful to Huiqiu Yuan for sending us the high-quality experimental data reproduced in Fig. 22.

This work granted me two awards. In 2020, it won the Best Poster presentation at the yearly encounter of the Brazilian Society of Physics; and, in 2020, the USP Graduate Video Award (Exact and Earth Sciences)[‡]. I am thankful for these recognitions, as they motivated me to work harder.

Finally, I am lucky to have my husband, Gabriel, my mom Fabiana, my dad Carlos and my sister Ana Laura. Even when far apart, their support was felt in every step while doing this thesis.

[‡] https://www.youtube.com/watch?v=zQKs6ZsR3VQ

"Mary wished to say something very sensible, but knew not how."

Pride and Prejudice - Jane Austen

ABSTRACT

FERRARI, A. L. R. F. **Real-space formulation of the numerical renormalization group method (NRG)**. 2022. 87p. Dissertation (Master of Science) - Instituto de Física de São Carlos, Universidade de Sao Paulo, São Carlos, 2022.

The equilibrium transport properties of an elementary nanostructured device with side-coupled geometry are computed and related to universal functions. The computation relies on a real-space formulation of the numerical renormalization-group (NRG) procedure. The real-space construction, dubbed eNRG, is more straightforward than the NRG discretization and allows more faithful description of the coupling between quantum dots and conduction states. The procedure is applied to an Anderson-model description of a quantum wire side-coupled to a single quantum dot. A gate potential controls the dot occupation. In the Kondo regime, the electrical conductance through this device is known to map linearly onto a universal function of the temperature scaled by the Kondo temperature. Here, the energy moments from which the Seebeck coefficient and the thermal conductance can be computed are shown to map linearly onto universal functions also. The moments and transport properties computed by the eNRG procedure are shown to agree very well with these analytical developments. Algorithms facilitating comparison with experimental results are discussed. As an illustration, one of the algorithms is applied to thermal dependence of the thermopower measured by Köhler in $Lu_{0.9}Yb_{0.1}Rh_2Si_2$, and to resistivity measurements in $CeRh_6Ge_4$. [1,2]

Keywords: Side coupled device. NRG. Universality.

RESUMO

FERRARI, A. L. R. F. **Formulação no espaço real do grupo de renormalização numérico (NRG)**. 2022. 87p. Dissertação (Mestre em Ciências) - Instituto de Física de São Carlos, Universidade de Sao Paulo, São Carlos, 2022.

As propriedades de transporte no equilíbrio de um dispositivo nanoestruturado elementar, com geometria de acoplamento lateral, são calculadas e relacionadas com funções universais. O cálculo se baseia em uma formulação do Grupo de Renormalização Numérico (NRG) no espaço real. A construção no espaço real, chamada de Grupo de Renormalização Numérico Exponencial (eNRG), é mais direta que a do NRG e permite uma descrição fidedigna do acoplamento entre pontos quânticos e estados de condução. Nós aplicamos o método ao modelo de Anderson, que descreve um ponto quântico lateralmente acoplado a um fio quântico. Um potencial de sítio controla a ocupação eletrônica no ponto quântico. No regime Kondo, a condutância elétrica se mapeia linearmente em uma função universal da temperatura. Aqui, mostramos que os momentos energéticos, a partir dos quais calculamos a condutância térmica e o coeficiente de Seeback, também se mapeiam linearmente em funções universais. Os momentos e propriedades de transportes calculados pelo eNRG concordam muito bem com esses resultados analíticos. Além disso, desenvolvemos algoritimos que facilitam a comparação com resultados experimentais. Dentre eles, está o estudo da dsependência térmica do coeficiente de Seeback, medida por Köhler em $Lu_{0.9}Yb_{0.1}Rh_2Si_2$.[1]

Palavras-chave: Dispositivo de acoplamento lateral. NRG. Universalidade.

CONTENTS

1

Introduction

The Numerical Renormalization Group method established its relevance when it provided a non-perturbative solution to the Kondo problem, ultimately explaining the observations of a resistivity minimum in magnetic alloys. [3–5] Today, the method has broad applicability and can also provide transport and excitation properties. [6] Thus, it has never lost its relevance: its precision and efficiency make it an excellent instrument for nano-device development and a state-of-the-art impurity solver for Dynamical Mean Field Theory. [7,8]

Since its creation in 1975, many modifications have improved the original NRG. Some examples are the interleaved-NRG, which proposes a new energy space discretization that increases numerical efficiency for multi-band problems, and the "open Wilson chains," which account for truncated bath modes by systematically defining an effective bath for each chain site. [9–11] In common, these modifications have the fact that they preserve the standard NRG scheme. They perform a logarithmic discretization of the conduction band, a Lanczos transformation, and truncation, then define the renormalization group transformation - all in energy space. Moreover, while they have undeniable numerical or precision gains, they come with a cost: simplicity.

The original energy space construction perfectly suits two of the most studied elementary devices. The side coupled device, a quantum dot side coupled to a quantum wire (SCD), and the single electron transistor (SET), two baths connected by a quantum dot, are efficiently described in terms of truncated block states of their baths. The reason is that the standard NRG transformation of the conduction band leaves the conduction band-impurity tunneling parameter unchanged, as it does not depend on momentum for these simple models. In addition, any momentum dependence does not contribute to their universal physical properties because these energy dependant terms are irrelevant operators in the renormalization group framework. [12]

With advancements in nanodevice construction, more elaborate geometries arise that are better represented by a real space description. In such devices, it is not atypical

that couplings have a strong momentum dependence, which may introduce marginal or relevant operators. [13] Consequently, NRG loses its remarkable precision. The logarithmically discretized energy space can no longer faithfully describe the original conduction band. Due to the relevance of this topic, other approximations have been developed to circumvent this problem. [6] Once again, simplicity was the price to pay.

Simplicity is a cornerstone of physics because it optimizes our description of the universe and allows us to see beyond irrelevant complications of a particular approach. This idea alone was our primary motivation for developing the exponential Numerical Renormalization Group, and it is arguably its main advantage. This method treats elaborate nanodevices naturally by discretizing the conduction band in real space. The result is analogous to the standard NRG discretization because it also allows an iterative diagonalization scheme. However, while NRG creates one discrete level for each portion of a logarithmically divided band, our discretization is more straightforward. Here, we divide sites into exponentially growing blocks and define one new operator for each block. It is because of this exponential growth that the method is called exponential-NRG.

All virtues of the standard NRG discretization are also present in eNRG: we have a rapid convergence to the continuum limit, uniform parameter-independent precision, and relatively small computational cost. The eNRG technical advantage appears at high temperatures, where the methods differ. Because we work in real space, no low energy approximation on the dispersion is necessary. Accordingly, we have a more accurate description of high energies or high temperatures. We will exemplify this assertion by comparing the conductance of a non-interacting SCD for the original bath, and the NRG/eNRG discretized baths.

The focus of this thesis is the eNRG method. Therefore, we chose to apply it to a well-known model and geometry, not to divert attention from the technique itself. Here, we will study the zero-bias transport properties of the SCD modeled by the Single-Impurity Anderson Model. The extensive universality studies of its physical properties in the Kondo regime provide an analytical benchmark for the eNRG. [14,15] In addition, we also show how these analytical results help interpret and find Kondo-physics signatures on experimental data.

We divide this thesis into four chapters. Chapter 2 defines the SIAM, the SCD, the relationship between this model and Kondo physics, and the Kondo regime. Its purpose is to sort out our application and basic physical principles so we can focus on developing the eNRG method in Chapter 3. This next chapter begins with an overview of Wilson's NRG formulation, then explains and derives our new approach and compares them. In addition, there is also a section detailing the implementation of the eNRG code in python to accompany the open source code. Then, Chapter 4 presents the three thermoelectric

properties we compute, i.e., the conductance, thermal conductance, and thermopower. It also explains how analytical calculations – denoted universality studies – benchmark eNRG results. Finally, Chapter 5 contains thermoelectric properties computed via eNRG and confirms the new method indeed works, because it agrees with our analytical results and experimental data.

Model

Quantum dots and wires are electronic structures of reduced size, in which quantum-size effects are fundamental. Electronic confinement at the nanometric scale leads to a discrete energy spectrum, as it does in quantum wells. With the quantum dot and wire as building blocks and considering electronic tunneling, we can construct more complex devices, as the Single-Electron-Transistor (SET) and Side-Coupled-Device (SCD), our object of study.

A high number of degrees of freedom interact in correlated systems. Ergo, we use Model Hamiltonians: they only account for relevant contributions to the description, simplifying the treatment. The single impurity Anderson model is used to describe one impurity coupled to a non-interacting conduction band. This model suits the Side-Coupled Device, with the impurity part representing the quantum dot, and the conduction band representing the quantum wire. The Hamiltonian is $H = H_{cb} + H_{imp} + H_{int}$.

The first term is

$$H_{cb} = -t \sum_{\sigma=\uparrow,\downarrow} \sum_{l\in\mathcal{L}} \left(c_{l,\sigma}^{\dagger} c_{l+1,\sigma} + H.c. \right), \tag{2.1}$$
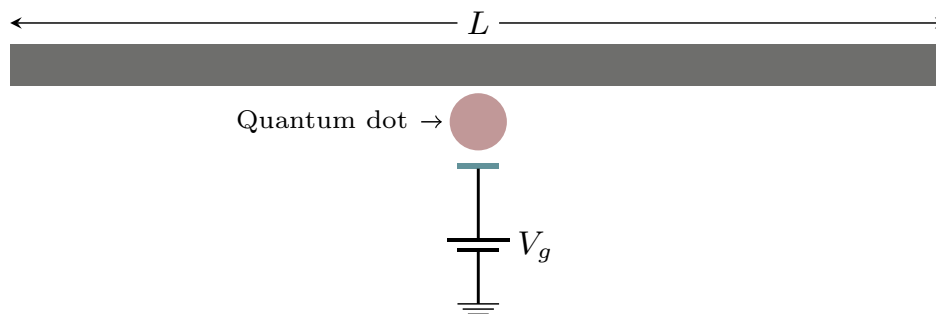

Figure 1 – Side coupled device. We divide the quantum wire in L sites, where L is an odd number. Electrons from the wire can tunnel into the quantum dot, where a gate potential V_g controls the occupation number.
Source: By the author.

where $\mathcal{L} = \left[-\frac{(L-1)}{2}, ..., \frac{(L-1)}{2}\right]$ represents the possible odd-L sites. It describes the quantum wire, i.e., the non-interacting conduction band, in a tight-binding approximation with nearest-neighbor hopping. In the SCD of Fig 1, the the dot Hamiltonian H_{imp} corresponds to our "Anderson impurity Hamiltonian". Its contribution is

$$H_{imp} = V_g(n_{d\uparrow} + n_{d\downarrow}) + Un_{d\uparrow}n_{d\downarrow}, \tag{2.2}$$

with an on-site potential V_g controlling the orbital occupation number by competing with the Coulomb repulsion ($U > 0$). The spacial confinement of the dot is responsible for the relevant Coulomb repulsion, neglected in the wire Hamiltonian. The quantum dot holds one energy level, which means it has, at most, a double occupation.

The last contribution

$$H_{int} = V \sum_{\sigma=\uparrow,\downarrow} \left(d_\sigma^\dagger c_{0,\sigma} + H.c.\right), \tag{2.3}$$

is the hybridization term. It allows electron tunneling between the dot and the wire.

2.1 Even-Odd Transformation

We simplify the numerical treatment of the model Hamiltonian by exploring the inversion symmetry of the SCD. As the device is symmetric around the quantum dot, it has even and odd wavefunctions. Odd wavefunctions are zero on the central site, and therefore, do not interact with the quantum dot. Thus, it is possible to write the Hamiltonian as an interacting and non-interacting term. We find the two independent terms with a change of basis. The even-odd transformation is

$$\begin{aligned} a_{0,\sigma} &= c_{0,\sigma} \\ a_{\ell,\sigma} &= \frac{c_{\ell,\sigma} - c_{-\ell,\sigma}}{\sqrt{2}} \\ b_{\ell,\sigma} &= \frac{c_{\ell,\sigma} + c_{-\ell,\sigma}}{\sqrt{2}}. \end{aligned} \tag{2.4}$$

Written in the new basis, the Hamiltonian becomes $H = H_A + H_B$, where

$$\begin{aligned} H_A = &-\sqrt{2}t\sum_\sigma(a_{0,\sigma}^\dagger a_{1,\sigma} + H.c.) - t\sum_\sigma\sum_{\ell\in\mathcal{L}'}(a_{l,\sigma}^\dagger a_{\ell+1,\sigma} + H.c.) \\ &+ H_d + H_{wd}, \end{aligned} \tag{2.5}$$

and

$$H_B = -t\sum_\sigma\sum_{\ell\in\mathcal{L}'}\left(b_{\ell,\sigma}^\dagger b_{\ell+1,\sigma} + H.c.\right), \tag{2.6}$$

with $\mathcal{L}' = \left[1, ..., \frac{(L-1)}{2}\right]$. Therefore, by only working with the interacting part H_A, we reduce the number of sites by half.

2.2 Particle-Hole Transformation

The model presents yet another symmetry when the Hamiltonian does not change as we exchange particles and holes. We define the particle-hole transformation as

$$
\begin{aligned}
a_{\ell,\sigma} &\leftrightarrow (-1)^{\ell} a_{\ell,\sigma}^{\dagger} \\
d_{\sigma} &\leftrightarrow d_{\sigma}^{\dagger},
\end{aligned}
\tag{2.7}
$$

where creation operators and annihilation operators are interchanged, effectively swapping electrons and holes.

By applying the transformation Eq. 2.7 to the even Hamiltonian H_A, we obtain a transformed Hamiltonian $\bar{H}_A = H_{cb} + H_{int} + \bar{H}_{imp}$ with a transformed dot Hamiltonian

$$
\bar{H}_{imp} = (U - V_g)(n_{d\uparrow} + n_{d\downarrow}) + U n_{d\uparrow} n_{d\downarrow}.
\tag{2.8}
$$

The Hamiltonian H_A is invariant (symmetric) when $H_A = \bar{H}_A$, which occurs in the symmetric point of the parametric space. Since the particle-hole transformation only alters the quantum dot Hamiltonian, this point is defined by equating Eq. 2.2 and Eq. 2.8, or by

$$
V_g = -U/2.
\tag{2.9}
$$

Fig. 2 represents the system in the vicinity of the symmetric point. If the Hamiltonian were symmetric, the energetic cost to access the external columns, starting from the central ones, would be the same. In other words, the same amount of energy would be required to create one electron or one hole, which manifests the particle-hole symmetry. The figure depicts a slightly asymmetric Hamiltonian in the Kondo regime for low thermal or excitation energies $\mathcal{E}$. The inequality

$$
\max(\mathcal{E}, \Gamma) \ll (|V_g|, V_g + U, D),
\tag{2.10}
$$

where $\Gamma = \pi \rho V^2$, defines this regime, which is a crucial concept for studying universality, in section 4. In this case, the small energies Γ responsible for charge fluctuations at the quantum dot are irrelevant, and the occupation n_d is unity.

For temperatures below the Kondo temperature, represented by the energy interval Γ_K, the conduction band electrons screen the singly occupied impurity, forming the Kondo singlet. This low temperature, non-perturbative physics of the Anderson model led to the creation of the NRG. [5]
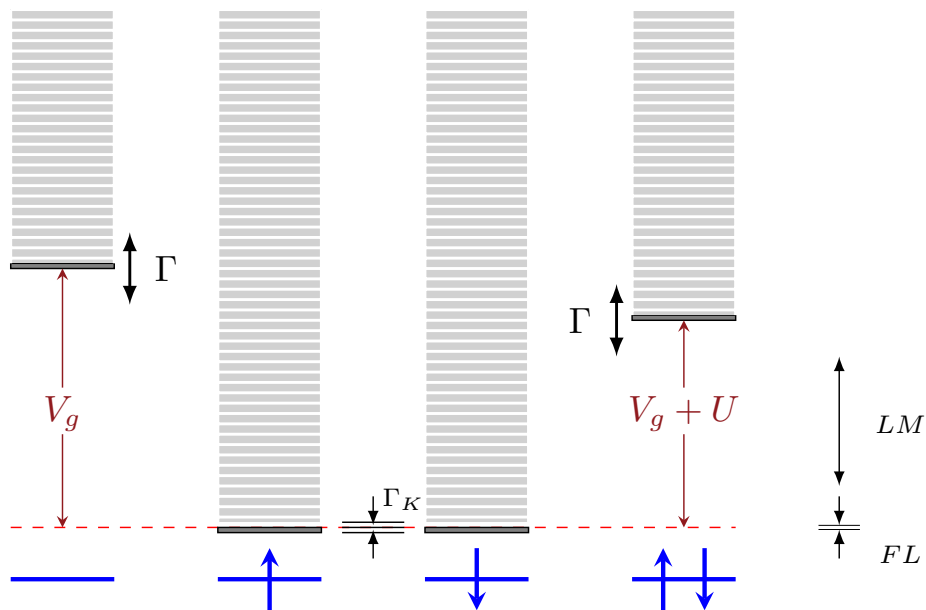
Figure 2 – Spectrum of the Anderson model near the symmetric point. The thick black lines represent the ground state for each dot configuration at the bottom, in blue. The columns above them are the possible excitations. When the hybridization is present ($V \neq 0$), the levels are widened (Γ), and the states mix between columns. The arrows represent the RG fixed-points of the Hamiltonian. The ground state is the Kondo singlet at thermal excitations below the energy width Γ_K, defined by the Kondo temperature.

Source: By the author.

3

Numerical Renormalization Group Methods

The NRG method provides an efficient non-perturbative solution to quantum impurity systems. Even though it is historically associated with the Kondo problem, its applications are more general. It can be applied to systems where a quantum mechanical impurity is coupled to a non-interacting bath of fermions or bosons. [16] There is extensive literature on NRG concepts and numerical implementations; therefore, in this section, we present an overview of the method, focusing on aspects where the eNRG departs from the standard NRG.[6,17]

3.1 The standard Numerical Renormalization Group

The first step in Wilson's NRG formulation is the logarithmic discretization of the conduction band in energy space, i.e.,

$$H_{cb} = \sum_{\sigma=\uparrow,\downarrow} \sum_{k} \varepsilon_k a_{k,\sigma}^{\dagger} a_{k,\sigma}. \tag{3.1}$$

Any numerical treatment of the infinite chain 3.1 would require some discretization, as it is impossible to implement infinite-dimensional matrices. Nevertheless, not all schemes produce good results, and there is an apparent reason why we must apply logarithmic discretization to quantum impurity systems. For instance, in the Kondo problem, the Kondo temperature defines an energy scale much smaller than those introduced by the model Hamiltonian. If the ratio between these energy scales is 10^5, a linear discretization would require energy intervals of order 10^{-6} for an appropriate resolution.[6] Unrealistically large matrices would provide such small energy intervals, resulting in an untreatable numerical problem. Wilson's discretization avoids the difficulty by only having a high resolution around the Fermi energy, where physical processes usually occur.

In the standard NRG scheme, we write the conduction band and the hybridization

Hamiltonians in an integral form, as

$$H_{cb} = \sum_\sigma \sum_{\alpha=R,L} \int_{-1}^{1} d\varepsilon \ g(\varepsilon)\varepsilon \ a^\dagger_{\varepsilon\alpha,\sigma} a_{\varepsilon\alpha,\sigma} \tag{3.2}$$

$$H_{int} = \sum_\sigma \sum_{\alpha=R,L} \int_{-1}^{1} d\varepsilon \ h(\varepsilon) \ (d^\dagger_\sigma a_{\varepsilon\alpha,\sigma} + H.c.), \tag{3.3}$$

where $a_{\varepsilon\alpha}$ are fermionic operators discribing the continuous conduction band, $g(\varepsilon)$ is the dispersion and $h(\varepsilon)$ is the hybridization between the impurity and the conduction band. To perform an even-odd transformation in the Hamiltonians, we define the operators

$$a_{\varepsilon,\sigma} = \frac{(a_{\varepsilon R,\sigma} + a_{\varepsilon L,\sigma})}{\sqrt{2}}, \tag{3.4}$$

and

$$b_{\varepsilon,\sigma} = \frac{(a_{\varepsilon R,\sigma} - a_{\varepsilon L,\sigma})}{\sqrt{2}}, \tag{3.5}$$

in terms of which they become

$$H_{cb} = \sum_\sigma \int_{-1}^{1} d\varepsilon \ g(\varepsilon)\varepsilon \ (a^\dagger_{\varepsilon,\sigma} a_{\varepsilon,\sigma} + b^\dagger_{\varepsilon,\sigma} b_{\varepsilon,\sigma}) \tag{3.6}$$

$$H_{int} = \sum_\sigma \int_{-1}^{1} d\varepsilon \ \sqrt{2}h(\varepsilon) \ (d^\dagger_\sigma a_{\varepsilon,\sigma} + H.c.). \tag{3.7}$$

The free conduction band described by the basis $\{b_\varepsilon\}$ does not interact with the impurity and can be disregarded. We proceed, as before, by working only with the basis $\{a_\varepsilon\}$.

We divide the continuous energy spectrum into intervals defined by

$$x_n = \pm\Lambda^{-n}, n = 0, 1, 2, 3..., \tag{3.8}$$

whose widths are given by

$$d_n = \Lambda^{-n}(1 - \Lambda^{-1}), \tag{3.9}$$

where the parameter $\Lambda > 1$ characterizes the discretization. Moreover, we recover the thermodynamic limit when $\Lambda \to 1$, with a continuous conduction band. Then, for each interval, we define one fermionic operator

$$a^\pm_{n,\sigma} = \pm\frac{1}{\sqrt{d_n}} \int_{x_{n+1}}^{x_n} d\varepsilon \ a_{\varepsilon,\sigma}. \tag{3.10}$$

We discretize the spectrum by projecting the initial basis $\{a_\varepsilon\}$ onto the newly defined incomplete basis $\{a^\pm_n\}$, that is,

$$a_{\varepsilon,\sigma} = \sum_n a^+_{n,\sigma} \Psi^+_n + a^-_{n,\sigma} \Psi^-_n, \tag{3.11}$$

with

$$\Psi_n^\pm = \begin{cases} \frac{1}{\sqrt{dn}}, & x_{n+1} < \pm\varepsilon < x_n, \\ 0, & \text{otherwise.} \end{cases} \tag{3.12}$$

This basis is incomplete with respect to the former because they do not have the same number of operators. This step is justified *a posteriori* by the rapid convergence of the physical properties to the continuum limit when $\Lambda \to 1$.[5]

The following step is writing the Hamiltonians in the new basis, starting from the interacting part Eq. 3.7. The first of Wilson's approximation considers a constant hybridization function $\Delta(\varepsilon)$. Accordingly, the function $h(\varepsilon)^2 = \Delta/\pi$ is also constant. We substitute the rewritten operators, Eq. 3.11, into the hybridization Hamiltonian 3.7, and it becomes

$$H_{int} = \sqrt{\frac{2\xi_0}{\pi}} \sum_\sigma \left(d_\sigma^\dagger f_{0,\sigma} + H.c. \right), \tag{3.13}$$

with

$$f_0 = \sqrt{\frac{\Delta}{\xi_0}} \sum_\sigma \sum_n \Lambda^{-n/2}(1 - \Lambda^{-1})^{1/2} \, (a_{n,\sigma}^+ + a_{n,\sigma}^-), \tag{3.14}$$

and

$$\xi_0 = \sum_n 2\Delta \, \Lambda^{-n}(1 - \Lambda^{-1}). \tag{3.15}$$

For simplicity, we started from the incomplete set of functions Eq. 3.12 to define the new basis Eq. 3.11. Nevertheless, it is straightforward to show that if we had started from a complete set of functions, exponentials with characteristic frequencies $\omega_n = 2\pi/d_n$, we would still end up with Eq. 3.13. Therefore, this equation is exact. And because the impurity-conduction band coupling is not affected by the discretization of the flat-conduction band, the NRG procedure is uniformly accurate for weak, moderate, or strong hybridizations.

The second approximation made in the standard NRG takes into consideration a linear dispersion $g(\varepsilon) = \varepsilon$. Once more, by direct substitution, this time into the conduction band Hamiltonian Eq. 3.6, we obtain

$$H_{cb} = \frac{(1 + \Lambda^{-1})}{2} \sum_\sigma \sum_n \Lambda^{-n}(a_{n,\sigma}^{+\dagger} a_{n,\sigma}^+ - a_{n,\sigma}^{-\dagger} a_{n,\sigma}^-). \tag{3.16}$$

Once discretized, the Hamiltonian must be mapped onto the Wilson chain. The goal is to find a new basis such that the Hamiltonian Eq. 3.16 becomes

$$H_{cb} = \sum_\sigma \sum_n \varepsilon_n f_{n,\sigma}^\dagger f_{n,\sigma} + \sum_\sigma \sum_n t_n(f_{n,\sigma}^\dagger f_{n+1,\sigma} + H.c.). \tag{3.17}$$

We determine the orthonormal basis $\{f_n\}$ via a Lanczos construction, starting from the operator f_0, Eq. 3.14. Thereby, the hybridization Hamiltonian, Eq. 3.13, maintains its

structure, where only one operator couples to the impurity. In order to find the coefficients ε_n and t_n, we define an orthogonal transformation between the basis $\{a_n^\pm\}$ and $\{f_n\}$, that is

$$a_{n,\sigma}^+ = \sum_m u_{mn} f_{m,\sigma}$$

$$a_{n,\sigma}^- = \sum_m v_{mn} f_{m,\sigma} \tag{3.18}$$

$$f_{m,\sigma} = \sum_n (u_{mn} a_{n,\sigma}^+ + v_{mn} a_{n,\sigma}^-).$$

Then, by equating the conduction band Hamiltonians, Eq. 3.16 and Eq. 3.17, and with the transformation above, we find recursive relations determining the coefficients u_{mn}, v_{mn}, t_n and ε_n.[18] Specifically, in the context of Wilson's approximations, these equations are exactly solvable, and we find no diagonal terms ($\varepsilon_n = 0$) and hopping coefficients

$$t_n = \frac{(1 + \Lambda^{-1})}{2} \frac{1 - \Lambda^{-n-1}}{\sqrt{1 - \Lambda^{-2n-1}}\sqrt{1 - \Lambda^{-2n-3}}} \Lambda^{-n/2}, \tag{3.19}$$

or

$$t_n \to \frac{(1 + \Lambda^{-1})}{2} \Lambda^{-n/2}, \tag{3.20}$$

in the limit of large n. The Hamiltonian that concludes this step is

$$H = \sum_\sigma \sum_n t_n (f_{n,\sigma}^\dagger f_{n+1,\sigma} + H.c.) + \sqrt{\frac{2\xi_0}{\pi}} (d_\sigma^\dagger f_{0,\sigma} + H.c.) + H_{imp}, \tag{3.21}$$

which now takes the simple form of a tight-binding chain with exponentially decreasing hopping coefficients, due to the logarithmic discretization.

We are now ready to define the Renormalization-Group (RG) scheme, starting from the Hamiltonian Eq. 3.21. We write it as a series of Hamiltonians

$$H = \lim_{N \to \infty} \Lambda^{-(N-1)/2} H_N, \tag{3.22}$$

where

$$H_\mathcal{N} = \Lambda^{(\mathcal{N}-1)/2} \left[\sum_\sigma \sum_{n=0}^{\mathcal{N}-1} t_n (f_{n,\sigma}^\dagger f_{n+1,\sigma} + H.c.) + \sqrt{\frac{2\xi_0}{\pi}} \sum_\sigma (d_\sigma^\dagger f_{0,\sigma} + H.c.) + H_{imp} \right], \tag{3.23}$$

and choose the scaling coefficients to cancel the N dependence on the last hopping t_{N-1} of each H_N. This choice ensures that the lowest energies are of order unity.

Eq. 3.23 is essential because it defines the RG transformation $H_{\mathcal{N}+1} = \mathcal{T}[H_\mathcal{N}]$, with

$$\tau[H_\mathcal{N}] = \sqrt{\Lambda} H_\mathcal{N} + \frac{(1 + \Lambda^{-1})}{2} (f_\mathcal{N}^\dagger f_{\mathcal{N}+1} + H. c.). \tag{3.24}$$

and admits an iterative diagonalization approach. We will come back to Eq. 3.24 after describing the eNRG method.

3.2   The exponential Numerical Renormalization Group

The alternative discretization we present is simple. All the critical characteristics of Wilson's procedure are present; however, we obtain the desired results by working in real space. This idea can be traced back to Wilson's original paper. Fig. 3 reproduces an image of said paper, where Wilson interprets the discretized NRG basis and reasons that the new operators – defined in energy space – correspond to shells in real space of increasing radius. As we move further away from the impurity along the Wilson chain, the shells acquire radius increments in powers of Λ. We invite the reader to keep this image in mind throughout this eNRG introduction, with the assurance we will go back to it in a few pages.

In the eNRG approach, once again, we must reduce the conduction band Hamiltonian to a tridiagonal form with exponentially decaying hopping coefficients. We start with the tight-binding Hamiltonian

$$H_{cb} = -\sqrt{2}t \sum_{\sigma}(a_{0,\sigma}^{\dagger}a_{1,\sigma} + H.c.) - t\sum_{\sigma}\sum_{\ell=1}^{\bar{L}}(a_{\ell,\sigma}^{\dagger}a_{\ell+1,\sigma} + H.c.), \qquad (3.25)$$

with $\bar{L} \to \infty$ in the continuum limit.

Two parameters control the discretization of the continuous conduction band within eNRG. The offset, denoted $\zeta \geq 0$, is a natural number that separates the Hamiltonian Eq. 3.25 into two parts, namely

$$H_{cb} = H_a + H_f. \qquad (3.26)$$

All sites with indices smaller than the offset ($\ell < \zeta$) are unaffected by the discretization, which will only impact the complementary part of the Hamiltonian. Therefore, the unchanged part of the Hamiltonian

$$H_a \equiv -t \sum_{\sigma}\left(\sqrt{2}\ a_{0,\sigma}^{\dagger}a_{1,\sigma} + \sum_{\ell=1}^{\zeta-1} a_{\ell,\sigma}^{\dagger}a_{\ell+1,\sigma} + H.c.\right) \qquad (3.27)$$

comprises the ζ first sites, plus the coupling to site ζ; and the portion to be discretized is

$$H_f \equiv -t\sum_{\sigma}\sum_{\ell=\zeta}^{\bar{L}}(a_{\ell,\sigma}^{\dagger}a_{\ell+1,\sigma} + \text{H. c.}). \qquad (3.28)$$

The second parameter, λ, is called the common ratio. Before providing its mathematical description, let us first look at the discretization scheme of Fig 4. The upper image has the minimum offset $\zeta = 0$, so the discretization affects all sites, while it starts from the second site in the lower image, which has $\zeta = 1$. In any case, we gather sites of
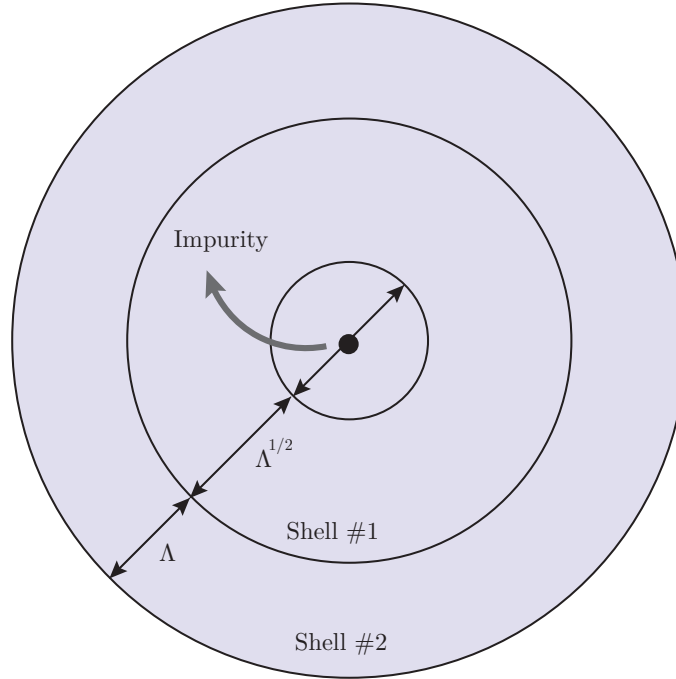
Figure 3 – Reproduction of Fig. 13 of Wilson's original paper. [5] Each spherical shell
represents the location of successive wave-functions in the Kondo basis. This
image connects the standard NRG to a real space representation.
Source: By the author.

the original chain into groups of increasing size λ^n ($n = 0,\ 1,\ 2,\ ...$) and define one new
operator f_n per group or *cell*. The common ratio controls the size of the n-th cell. The
number of sites in the first n cells is

$$\mathcal{G}_n \equiv \frac{\lambda^n - 1}{\lambda - 1}, \tag{3.29}$$

and the name becomes evident as $\mathcal{G}_n$ is the geometric series with a common ratio λ. In
the figure in question, we chose $\lambda = 2$. Furthermore, we recover the continuum limit with
$\lambda \to 1$, in which case $\mathcal{G}_n \to n$ and we have the original chain.

The new basis of normalized Fermi operators is

$$f_{n,\sigma} \equiv \sum_{j=1}^{\lambda^n} \alpha_{n,j} a_{n,j,\sigma} \qquad (n = 0, 1, \ldots), \tag{3.30}$$

with complex coefficients

$$\alpha_{n,j} = |\alpha_{n,j}| \exp(i\phi_{n,j}), \tag{3.31}$$

which must be normalized

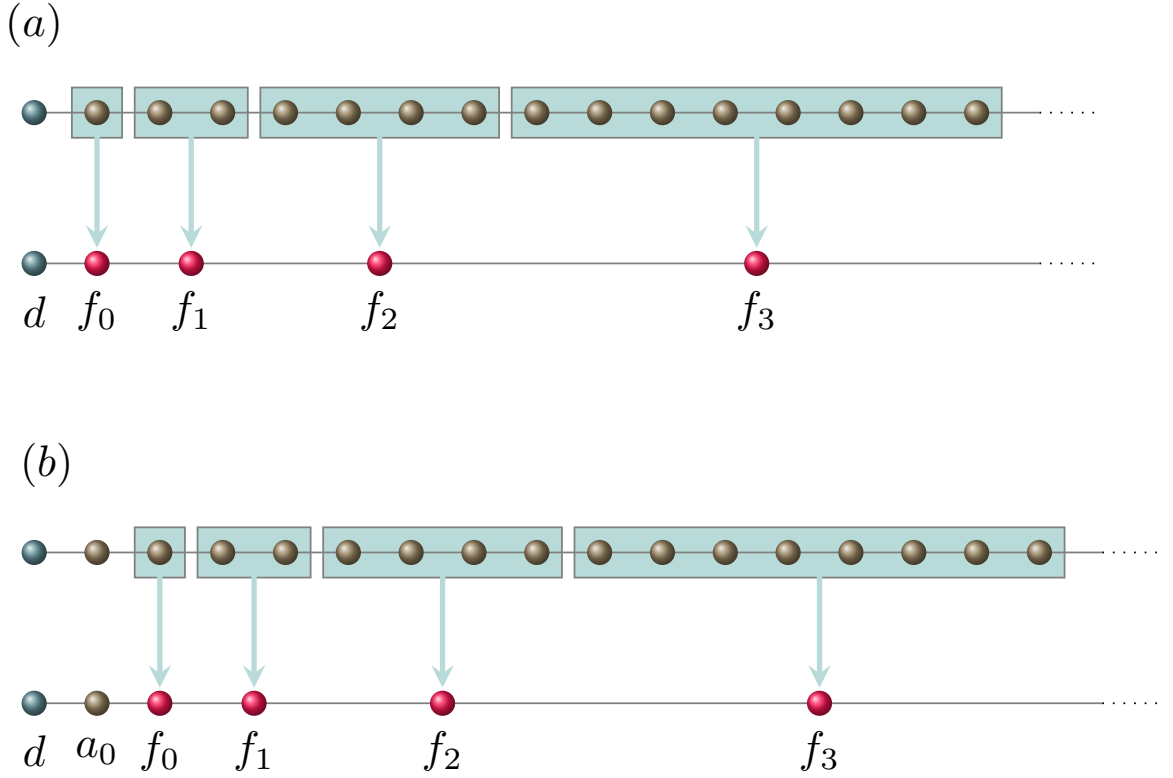$$\sum_{j=1}^{\lambda^n} |\alpha_{n,j}|^2 = 1. \tag{3.32}$$

Figure 4 – Representation of the real space discretization used in the modified NRG. Sites in the quantum wire are divided in groups of increasing size, and each group is represented by one operator of the new $\{f\}$ basis.
Source: By the author.

Although the operators Eq. 3.30 are mutually orthogonal, they are not a complete basis with respect to the original one, as the new basis does not have the same number of operators. Nevertheless, as in the standard NRG construction, we will proceed with this incomplete basis and justify the approximation *a posteriori* by the rapid convergence of physical properties in the continuum limit. In practice, we treat the transformation as orthonormal, and its inversion yields

$$a_{n,j,\sigma} = \alpha^*_{n,j} f_{n,\sigma} \qquad (n = 0, 1, \ldots; j = 1, 2, \ldots, \lambda^n). \tag{3.33}$$

We obtain the Hamiltonian

$$H_{f\lambda} \equiv -t \sum_{\sigma} \sum_{n=1}^{\infty} \sum_{j=1}^{\lambda^n - 1} (\alpha_{n,j} \alpha^*_{n,j+1} + \text{c. c.}) f^\dagger_{n,\sigma} f_{n,\sigma} - t \sum_{\sigma} \sum_{n=0}^{\infty} (\alpha_{n,\lambda^n} \alpha^*_{n+1,1} f^\dagger_{n,\sigma} f_{n+1,\sigma} + \text{H. c.}). \tag{3.34}$$

in the new basis by substituting Eq. 3.33 into Eq. 3.25. However, while the original Hamiltonian Eq. 3.25 has no diagonal terms, the first term on the right-hand side of Eq. 3.34 does not follow this prescription. Fortunately, we can eliminate this discrepancy by our phase choice

$$\phi_{n,j} = \frac{\pi}{2}(\mathcal{G}_n + n + j). \tag{3.35}$$

Appendix A.1 shows that by choosing this phase, we obtain the final Hamiltonian

$$H_{f\lambda} = t \sum_{\sigma} \sum_{n=0}^{\infty} \left(\left| \alpha_{n,\lambda^n} \right| \left| \alpha_{n+1,1} \right| f_{n,\sigma}^{\dagger} f_{n+1,\sigma} + \text{H. c.} \right). \tag{3.36}$$

with no inconsistencies.

The absolute values of the coefficients 3.31 are to be defined. Here, the only a priori condition is that they must satisfy 3.32. Yet, the infinite possible choices are not equally suitable. [19] Luckily, we do not need to look far to find coefficients that yield a Hamiltonian favorable to iterative diagonalization with fast decaying hoppings. Given the equivalence between lattice sites, the most simple and physically satisfactory choice already fulfills this goal. By selecting identical coefficients within a cell

$$\left| \alpha_{n,j} \right| = \alpha_n \qquad (j = 1, \ldots, \lambda^n), \tag{3.37}$$

their normalization condition yields

$$\left| \alpha_{n,j} \right| = \lambda^{-\frac{n}{2}}. \tag{3.38}$$

Finally, the discretized portion of the Hamiltonian becomes

$$H_{f\lambda} = \sum_{\sigma} \sum_{n=0}^{\infty} (t_n f_{n,\sigma}^{\dagger} f_{n+1,\sigma} + \text{H. c.}), \tag{3.39}$$

with hopping coefficients

$$t_n = t\lambda^{-n-\frac{1}{2}} \qquad (n > 0), \tag{3.40}$$

that quickly decay. We leave case $n = 0$ out from Eq. 3.40 because, as a consequence of the even-odd transformation, the first hopping coefficient of the non-discretized chain accompanies a $\sqrt{2}$. So, if $\zeta = 0$, we must account for this extra factor, i.e.,

$$t_0 = \begin{cases} \sqrt{2}t\lambda^{-\frac{1}{2}} & (\zeta = 0) \\ t\lambda^{-\frac{1}{2}} & (\zeta > 0) \end{cases}. \tag{3.41}$$

For the sake of completeness, we write the entire Hamiltonian

$$H_{A\lambda} = -t \sum_{\sigma} \left(\sqrt{2}a_{0,\sigma}^{\dagger} a_{1,\sigma} + \sum_{\ell=1}^{\zeta-1} a_{\ell,\sigma}^{\dagger} a_{\ell+1,\sigma} + a_{\zeta,\sigma}^{\dagger} f_{0,\sigma} + \text{H. c.} \right) + H_{f\lambda} + H_{dot} + H_{dc}. \tag{3.42}$$

The exponential decay of hopping coefficients allows definition of a renormalization-group transformation.[5] To this end, consider our energy scale of interest $\mathcal{E}$, and a dimensionless *infrared-truncation* parameter $\gamma \ll 1$. We search the smallest integer $\mathcal{N}$ satisfying the inequality

$$t\lambda^{-\mathcal{N}} < \gamma\mathcal{E}. \tag{3.43}$$

Substitution of $\mathcal{N} - 1$ for the upper limit of the sum then reduces the right-hand side of Eq. (3.39) to a finite series:

$$H_{f\lambda} = \sum_{\sigma} \sum_{n=0}^{\mathcal{N}-1} t_n(f_{n,\sigma}^\dagger f_{n+1,\sigma} + \text{H. c.}). \tag{3.44}$$

The inequality (3.43) controls the accuracy of this approximation. In the limit $\gamma \to 0$, Eq. (3.44) becomes equivalent to Eq. (3.39).

The right-hand side of Eq. (3.44) can now be substituted for $H_{f\lambda}$ on the right-hand side of Eq. (3.42). Next, the resulting finite series is scaled up by the factor $1/t_{\mathcal{N}-1} \equiv \lambda^{N-1/2}/t$, which yields the dimensionless, truncated Hamiltonian $H_{\mathcal{N}}$:

$$\begin{aligned} t_{\mathcal{N}-1} H_{\mathcal{N}} = H_{dot} + H_{dc} + \sum_{\sigma} \sum_{n=0}^{\mathcal{N}-1} t_n(f_{n,\sigma}^\dagger f_{n+1,\sigma} + \text{H. c.}) \\ - t \sum_{\sigma} \left(\sqrt{2} a_{0,\sigma}^\dagger a_{1,\sigma} + \sum_{\ell=1}^{\zeta-1} a_{\ell,\sigma}^\dagger a_{\ell+1,\sigma} + a_{\zeta-1,\sigma}^\dagger f_{0,\sigma} + \text{H. c.} \right). \end{aligned} \tag{3.45}$$

This truncation of the Hamiltonian is what allows its iterative diagonalization, which is detailed in Sec. 3.4. At a certain iteration, the *ultraviolet cutoff* sets an upper bound to the eigenvalues we compute, i.e., we discard states with energies greater than E_{uv}. Besides the many-body energy spectra, eNRG/NRG can also calculate matrix elements of the Fermi operators a_ℓ ($\ell = 0, \ldots, \zeta - 1$) and f_n ($n = 0, \ldots, \mathcal{N}$) between pairs of eigenvectors, with low computational effort. Moreover, Eq. (3.45) defines the renormalization-group transformation $\tau[H_{\mathcal{N}}] = H_{\mathcal{N}+1}$, which adds a smaller energy scale to $H_{\mathcal{N}}$ and rescales the result so that the resulting smallest eigenvalue be of $\mathcal{O}(1)$. From Eq. (3.45), it follows that

$$\tau[H_{\mathcal{N}}] = \lambda H_{\mathcal{N}} + \sum_{\sigma}(f_{\mathcal{N},\sigma}^\dagger f_{\mathcal{N}+1,\sigma} + \text{H. c.}). \tag{3.46}$$

We have reached the same point where we stopped the standard NRG description. The two methods, vastly distinct so far, meet each other in Eqs. 3.46 and 3.24. These equations are the starting point for the iterative diagonalization procedures, which are identical for both methods, except for the precise form of the hopping coefficients. So then our next step in this study is comparing both procedures to highlight their differences.

3.3   Comparison between procedures

Looking at Eqs. 3.24 and 3.46, one notices that the two approaches become equivalent when $\Lambda \to \lambda^2$. Under these conditions, the asymptotic form of the NRG hopping coefficients matches the eNRG result Eq. 3.40, which is a much neater expression for t_n. The correspondence between methods is shown in Fig. 5, where we plot both approaches'
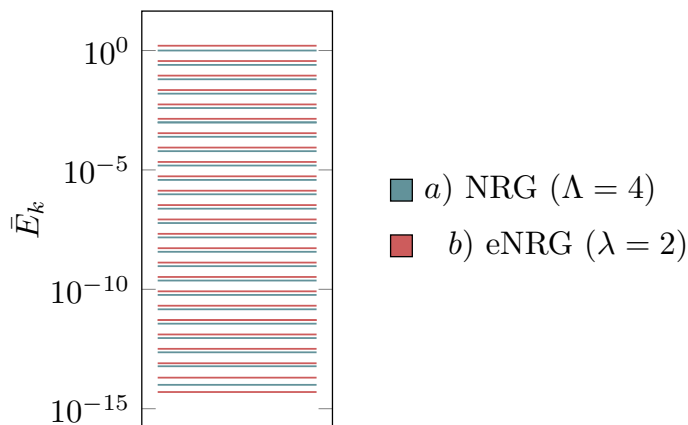
Figure 5 – Conduction band positive energy spectra in logarithmic scale. *a*) Wilson's discretization, with $\Lambda = 4$. *b*) Real space discretization. The new discretization exhibits the correct behavior: its spectrum is uniformly spaced on a logarithmic scale. Hence, it has a high energy resolution around the Fermi level.
Source: By the author.

discretized conduction band spectra. The figure shows the eNRG yields uniformly spaced energies in a log scale, proving we are also working with a logarithmically discretized conduction band in eNRG. Furthermore, we are now equipped to go back to Fig. 3. We can regard the eNRG as the formal implementation of Wilson's wavefunctions shells. In fact, the correspondence is remarkable, as the eNRG cells grow precisely like the Onion-like spherical shells in Wilson's original paper. Fig. 6 draws attention to this parallel by superposing Figs. 3 and 4.

In both NRG approaches, the parameters Λ and λ characterize the discretization: they set the accuracy and velocity of the calculations. In this thesis, we chose to present a simplified version of our method, where we so far discussed the common ratio λ as a natural number. If this were the case, we would have a manifest discrepancy between the approaches and a disadvantage of the eNRG since a natural λ limits our control over the accuracy-velocity balance. However, this is not the case for two reasons. First, we can formally expand the common ratio to real $\lambda \geq 1$.[19] Second, this expansion was unnecessary for all of our calculations, where $\lambda = 2$ provided results with standard NRG accuracy and comparable numerical efficiency.

To show the numerical equivalence, let us compare computation times for a symmetric model with Coulomb repulsion $U = t$ and dot-level width $\Gamma = 0.4\,t$, when computing the three energy moments $\mathcal{L}_j$ ($j = 0, 1, 2$). We chose parameters so that the results for conductance had less than 1% difference for every temperature. A C++ algorithm runs NRG with $\Lambda = 4$ and $E_{\mathrm{uv}} = 40\,t$, and eNRG with $\lambda = 2$, $E_{\mathrm{uv}} = 40\,t$, and $\zeta = 1$ in approximately 140s. Our unoptimized Python code runs the identical computation in
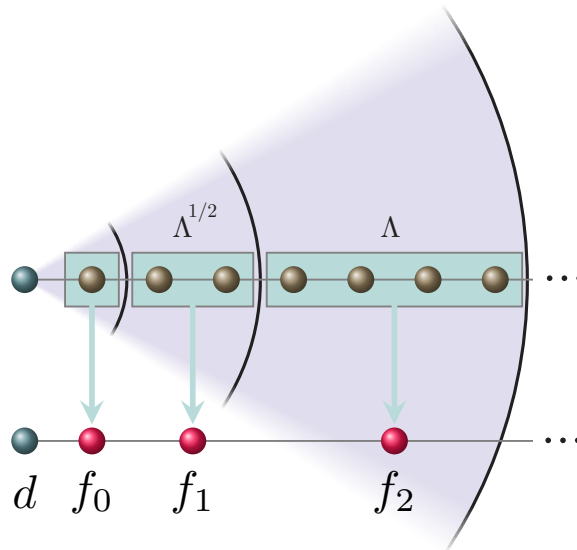
Figure 6 – This figure illustrates the resemblance between Wilson's shell interpretation of the NRG operators and the eNRG discretization. Interestingly, our shells increase in size as he predicted, which becomes clear once we realize $\Lambda = \lambda^2 = 4$ in this example.
Source: By the author.

approximately 500s. Concerning computational cost, the eNRG and NRG procedures are equivalent. Details of our implementation are in Sec. 3.4.

In Wilson's method, $\Lambda \to 1$ recovers the continuum spectrum as the widths Eq. 3.9 approach zero in each interval, in which case the calculations would take infinite time. As Λ increases, there is a loss in accuracy and gain in computation time. If $\Lambda \lesssim 3$, Wilson argued that the numerical errors were unimportant when computing thermodynamical averages. For $\Lambda > 4$, errors introduce characteristic oscillations in plots of physical quantities versus temperature, with period $\log(\Lambda)$.[5] The z-averaging provides a way around the problem: it yields precise results in little time, and allows discretization parameters as big as $\Lambda = 10$.[20] Because the methods are equivalent when $\lambda^2 = \Lambda$, the typical value of $\lambda = 2$ already presents oscillations in thermodynamic averages and requires a modified version of the z-average.

In the eNRG, there are two ways to remove the artificial oscillations. The first one, used in all plots presented in this thesis, is to average results with offsets $\zeta = 0$ and $\zeta = 1$. As we show in Appendix A.2, $\zeta = 0$ corresponds to $z = 1$, and $\zeta = 1$ corresponds to $z = 1.5$. While this was enough for our present application, not having a way to describe real z is a severe limitation to computing excitation properties, as we need to differentiate with respect to z.[20] Therefore, we developed a third discretization parameter $\omega \in \mathbb{R}$ to evade this issue.[19] Albeit a critical addition to eNRG, the extension is not particularly
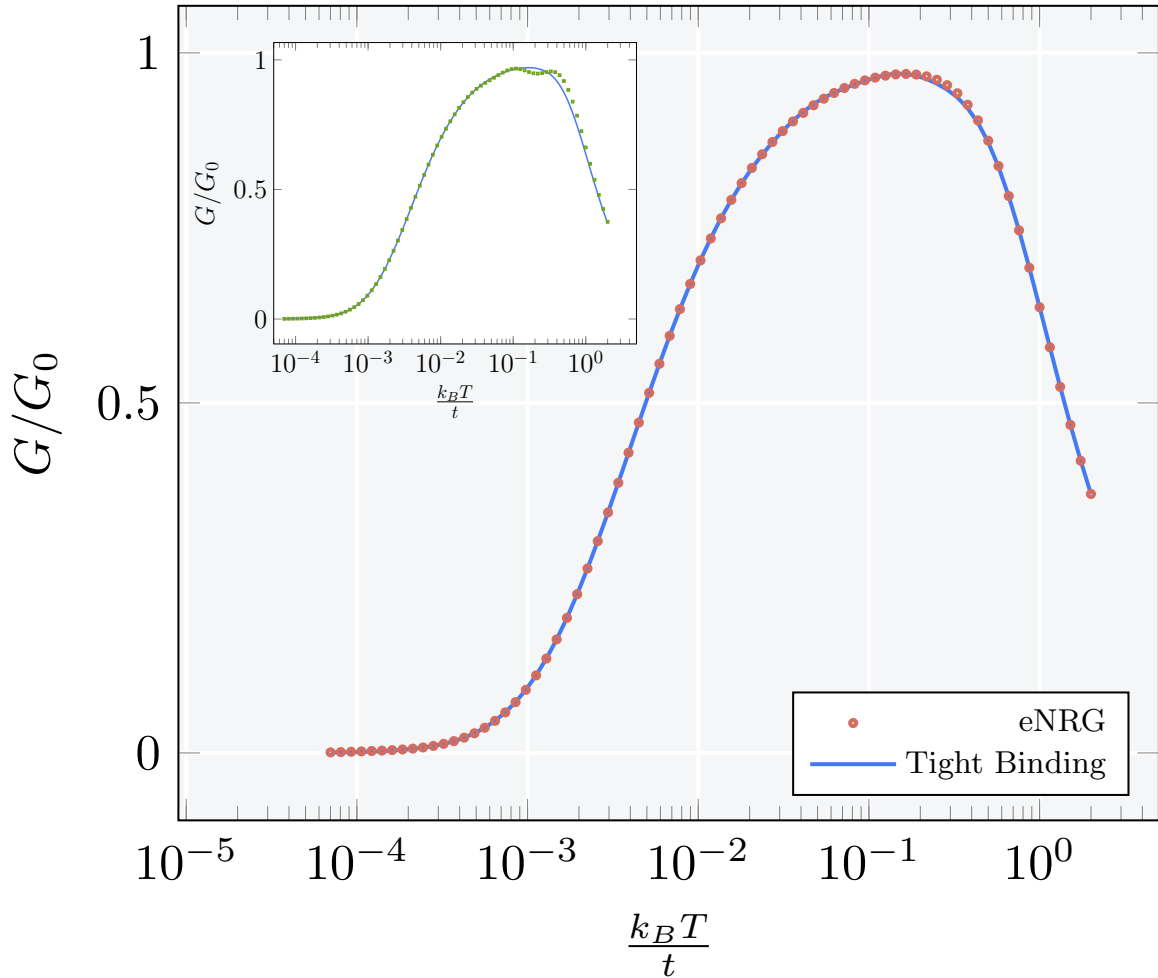
Figure 7 – Thermal dependence of the conductance for the $U = V_g = 0$ model, with level width $\Gamma = 1 \times 10^{-2} t$. The red circles are eNRG results, as the label describes. Each circle represents the average of two computations with $\lambda = 2$, for offsets $\zeta = 3$ and $\zeta = 4$. The solid line resulted from numerically diagonalizing the ($\lambda = 1$) tight-binding Hamiltonian for $L = 2001$. The inset shows the same calculation for the NRG, where the green squares show the average over z of two computations with $\Lambda = 4$, for $z = 0.5$ and $z = 1$.
Source: By the author.

important for this thesis — where we only compute transport properties.

The offset, a concept so naturally introduced in the eNRG, goes beyond eliminating oscillations in thermodynamic properties. In fact, keeping larger energy scales in the Hamiltonian improves the description of high energies/temperatures. In more technical terms, it systematically decreases high-temperature deviations introduced by irrelevant operators stemming from the discretization. Interestingly, this is easily shown by a non-interacting model.

The non-interacting Hamiltonians Eqs. 3.45 and 3.23 are quadratic and can be normally diagonalized, which returns their eigenvalues and eigenvectors. For the $U = 0$ side coupled device, the expression for electrical conductance is

$$G(T) = \frac{G_0}{\rho} \sum_{\sigma,n} \{a_{0,\sigma}^\dagger, g_{n,\sigma}\}^2 \left(-\frac{\partial f_\beta(\epsilon)}{\partial \epsilon} \right)_{\epsilon=\mathcal{E}_n} , \qquad (3.47)$$

where $G_0 = 2e^2/h$ is the conductance quantum, $\mathcal{E}_n$ is the energy associated to the eigenoperator g_n, and

$$f_\beta(\epsilon) = \frac{1}{1 + \exp\{\beta\epsilon\}} \qquad (3.48)$$

is the fermi function.[21]

The main plot in Fig. 7 shows the conductance, Eq. 3.47, calculated via the eNRG Hamiltonian. The solid line has a common ratio $\lambda = 1$, yielding the original tight-binding Hamiltonian (Eq. 3.25) with size L' (thermodynamic limit). Near the Fermi level, it has approximately uniform spacing $\Delta E = 2\pi/L'$, so we choose a large system size $L' = 10^4$ to describe temperatures $k_B T > 1 \times 10^{-3} t$ accurately. Thus, the solid line has no irrelevant operator problems because it represents the non-discretized model. The scattered circles in the same figure come from $\lambda = 2$ and have no oscillations because we average two offsets, $\zeta = 3$ and $\zeta = 4$. The inset shows calculations with the same parameters stemming from the NRG Hamiltonian. Again, the solid lines represent the thermodynamic limit, which means conductances computed with $\Lambda = 1.0001$ and $\mathcal{N} = 10^4$. The green squares show results for the NRG discretization, with $\Lambda = 4$ and $\mathcal{N} = 40$.

Although the solid lines come from the continuum limits of the two approaches, they are practically the same. However, a significant discrepancy is present in the scattered points. While the eNRG calculation is in excellent agreement with the non-discretized Hamiltonian, there are significant deviations in the inset for $k_B T > 0.1t$. The inaccuracy of NRG, of $\mathcal{O}(k_B T/D)$, stems from irrelevant operators introduced by the logarithmic discretization. The eNRG does not have this problem because a large offset means we faithfully describe high energy degrees of freedom.

3.4   Numerical implementation

This section aims to guide the reader through our eNRG python code, available at Github*. Readers interested in using our code or learning about the eNRG implementation will benefit from this section. It is not vital for comprehending the rest of this thesis.

The first step in solving a problem requiring the diagonalization of a Hamiltonian is exploring its symmetries. Three conserved quantities of the Anderson Hamiltonian will aid our implementation: particle number and spin, and the spin projection S_z. Consequently, for any NRG iteration, our Hamiltonians will be divided into block-diagonal subspaces of the same charge (Q) and spin (S). Inside each subspace, states with different values of S_z are degenerate. Thus, we only need to take into account one value of s_z, and for simplicity, we take the maximum one. Moreover, a standard definition in the NRG literature is to define half-filling as $Q = 0$.

Let us look at the Hamiltonian (SIAM) of the first eNRG iteration to exemplify these concepts. The shortest possible Wilson chain contains two sites: the impurity and one bath site. The state with a maximum charge has four electrons, the state with a minimum charge has none, and the half-filled state has two electrons. Thus, Q ranges from $-2 \leq Q \leq 2$.

Our basis states also have to be eigenstates of the spin operator. We have no spin when we have no electrons, so ($Q = -2, S = 0$) is the first subspace we find. By adding one electron, the only possibility for the spin is $S = 1/2$, so the next viable subspace is ($Q = -1, S = 1/2$). When two states with $S = 1/2$ are added, there are only two possibilities for the spin, i. e. $S = 0$ and $S = 1$. Hence, the half-filled subspaces are ($Q = 0, S = 0$) and ($Q = 0, S = 1$). Following the same procedure for all states, we discover all possible subspaces for the first eNRG iteration and notice they have the checker-board structure in Fig. 8. In the implementation, it is crucial to easily identify the labels of a subspace. We achieve this effortlessly if we pay attention to the ordering of the Hamiltonian blocks, which are the arrows in the figure, and this ordering scheme is denoted *diagonal ordering*.

The Hamiltonian H_0 and its basis are shown in Eq. 3.49 and Tab. 1 respectively. We remind the reader that the parameters V, V_g and U were defined, along with the model, in Sec. 2. As already mentioned, because the Hamiltonian has rotational invariance, we only need to perform the diagonalization for states with maximum s_z. For this reason, our initial basis is restricted to just 10 states.

---

*   https://github.com/anarfferrari/Python-eNRG-code

Table 1 – Primitive basis for constructing the first iteration Hamiltonian H_0. Notice how all states have the maximum value of s_z given their spin subspace.

Subspace (Q, S)	Basis $N = 0$
$(2, 0)$	$d_\uparrow^\dagger d_\downarrow^\dagger f_{0,\uparrow}^\dagger f_{0,\downarrow}^\dagger \lvert\emptyset\rangle$
$(1, 1/2)$	$d_\uparrow^\dagger f_{0,\uparrow}^\dagger f_{0,\downarrow}^\dagger \lvert\emptyset\rangle \, , \ d_\uparrow^\dagger d_\downarrow^\dagger f_{0,\uparrow}^\dagger \lvert\emptyset\rangle$
$(0, 0)$	$\frac{1}{2}\left(d_\uparrow^\dagger f_{0,\downarrow} - d_\downarrow^\dagger f_{0,\uparrow}\right)\lvert\emptyset\rangle \, , \ d_\uparrow^\dagger d_\downarrow^\dagger \lvert\emptyset\rangle \, , \ f_{0,\uparrow}^\dagger f_{0,\downarrow}^\dagger \lvert\emptyset\rangle$
$(0, 1)$	$d_\uparrow^\dagger f_{0,\uparrow}^\dagger \lvert\emptyset\rangle$
$(-1, 1/2)$	$d_\uparrow^\dagger \lvert\emptyset\rangle \, , \ f_{0,\uparrow}^\dagger \lvert\emptyset\rangle$
$(-2, 0)$	$\lvert\emptyset\rangle$

Source: By the author.

$$H_0 = \begin{pmatrix} 0 & & & & & & & & \\ & V_g & V & & & & & & \\ & V & 0 & & & & & & \\ & & & V_g & & & & & \\ & & & & 2V_g + U & -\sqrt{2}V & 0 & & \\ & & & & -\sqrt{2}V & V_g & -\sqrt{2}V & & \\ & & & & 0 & -\sqrt{2}V & 0 & & \\ & & & & & & & 2V_g + U & -V \\ & & & & & & & -V & V_g \\ & & & & & & & & & 2V_g + U \end{pmatrix} \tag{3.49}$$

After constructing and diagonalizing the Hamiltonian of the first iteration, we must add the following site and build the next Hamiltonian. The small matrix H_0 was computed by hand; however, we need to automate this process. We begin by constructing the new basis by adding a site to the previous basis of eigenstates, i.e. to the *eigenbasis*. Let us say we know the eigenvalues and eigenvectors $E_{N-1}^{Q,S,\ell}$ and $\lvert Q, S, S_z, \ell\rangle_{N-1}$, where ℓ differentiates states inside a subspace, and we bring back the index S_z for the following discussion.

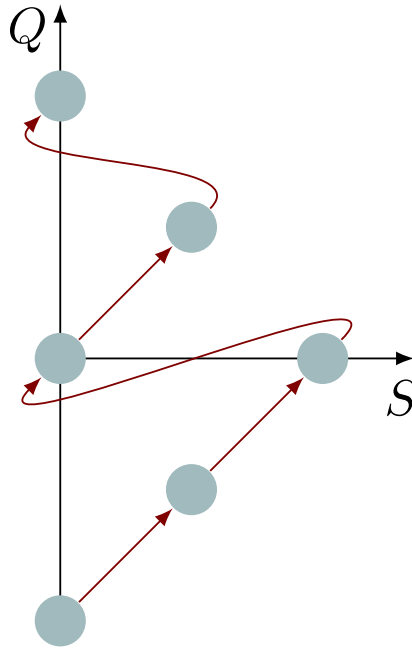Notice that by adding one site in the Wilson chain, we redefine half-filling, and

Figure 8 – Checker-board structure of the subspaces of $N = 0$, and definition of diagonal ordering.
Source: By the author.

hence, Q. For example, $|\uparrow, \uparrow\rangle$ is half-filled, but it is one electron short of half-filling in $|\uparrow, \uparrow, \cdot\rangle$. If we add an empty site, the state does not change, but the labels do. Hence, the first type of new basis state is

$$|Q - 1, S, S_z, p_1\rangle_N^{\mathcal{S}} = \mathcal{O}_S |Q, S, S_z, \ell\rangle_{N-1} \tag{3.50}$$

The corresponding operator is labeled $\mathcal{S}$ because the new state belongs to a subspace to the *south* of the one that generates it: its *parent subspace*. Fig 9. aids the understanding of this assertion. By applying the south operator to a state belonging to the subspace in blue of iteration $N - 1$, we generate states on the subspace directly below it, in red, of iteration N. Furthermore, notice that we restrict the label ℓ (Eq. 3.50) to the eigenstates and the label p_i to the new state, which is not an eigenstate. The states denoted by p_i for the *primitive basis*. Similarly, we can add a site f_N with two electrons, and we obtain states with the north operator

$$|Q + 1, S, S_z, p_2\rangle_N^{\mathcal{N}} = \mathcal{O}_N |Q, S, S_z, \ell\rangle_{N-1}. \tag{3.51}$$

Adding a site with one electron is slightly trickier as the resulting state must be an eigenstate of the spin operator. Beginning with the subspace (Q, S), the new state must be in the subspace $(Q, S \pm 1/2)$. We have the liberty of choosing any value of S_z that seems fit due to symmetry, and we select

$$\left|Q, S - \frac{1}{2}, S_z - \frac{1}{2}, p_2\right\rangle_N^{\mathcal{W}} = O_{\mathcal{W}} |Q, S, S_z, \ell\rangle_{N-1}, \tag{3.52}$$

and

$$|Q, S + \frac{1}{2}, S_z + \frac{1}{2}, p_3\rangle_N^{\mathcal{E}} = O_{\mathcal{E}} |Q, S, S_z, \ell\rangle_{N-1}, \tag{3.53}$$

In concrete terms, the new states and operators are defined by

$$\mathcal{O}_{\mathcal{S}} |Q, S, S_z, \ell\rangle_{N-1} \equiv |Q, S, S_z, \ell\rangle_{N-1}, \tag{3.54}$$

$$\mathcal{O}_{\mathcal{N}} |Q, S, S_z, \ell\rangle_{N-1} \equiv f_{N\uparrow}^{\dagger} f_{N\downarrow}^{\dagger} |Q, S, S_z, \ell\rangle_{N-1}, \tag{3.55}$$

$$\mathcal{O}_{\mathcal{W}} |Q, S, S_z, \ell\rangle_{N-1} \equiv \begin{pmatrix} S - \frac{1}{2} & \frac{1}{2} & S \\ S_z - \frac{1}{2} & \frac{1}{2} & S_z - 1 \end{pmatrix} f_{N\uparrow}^{\dagger} |Q, S, S_z - 1, \ell\rangle_{N-1}$$

$$+ \begin{pmatrix} S - \frac{1}{2} & \frac{1}{2} & S \\ S_z - \frac{1}{2} & -\frac{1}{2} & S_z \end{pmatrix} f_{N\uparrow}^{\dagger} |Q, S, S_z, \ell\rangle_{N-1}, \tag{3.56}$$

and

$$\mathcal{O}_{\mathcal{E}} |Q, S, S_z, \ell\rangle_{N-1} \equiv \begin{pmatrix} S + \frac{1}{2} & \frac{1}{2} & S \\ S_z + \frac{1}{2} & \frac{1}{2} & S_z \end{pmatrix} f_{N\uparrow}^{\dagger} |Q, S, S_z, \ell\rangle_{N-1}$$

$$+ \begin{pmatrix} S + \frac{1}{2} & \frac{1}{2} & S \\ S_z + \frac{1}{2} & -\frac{1}{2} & S_z + 1 \end{pmatrix} f_{N\downarrow}^{\dagger} |Q, S, S_z + 1, \ell\rangle_{N-1}, \tag{3.57}$$

where the matrices above denote the Clebsch-Gordan coefficients where spins (upper row) and spin projections (lower row) of the right-hand side combine to form the left-hand side.

We say that the eigenstate $|Q, S, S_z, \ell\rangle_{N-1}$ is the parent of four new basis states, with genders $\mathcal{N}, \mathcal{S}, \mathcal{W}, \mathcal{E}$. Fig. 9 shows this construction. Here, we see how one parent subspace creates child subspaces in the cardinal directions. In general, subspaces in the four directions are created, except for $S = 0$, where there is no possible subspace to the west. By keeping track of the genders, we know where the state came from (its parent). From the figure, it is also clear that the checker-board structure is maintained in further iterations. Therefore, the diagonal ordering is still well defined. Moreover, we see why even and odd iterations are often distinguished in NRG: only even iterations (in my definition of N) have the subspace $(Q = 0, S = 0)$.

In our code, it is not only the ordering of subspace blocks that matters but also the order of states inside a block. In particular, we order the basis of a specific $H_N^{Q,S}$ by

Table 2 – Useful definitions for the eNRG code.

Eigenbasis	Eigenstate of an iteration, labeled by the index ℓ. By operating $\mathcal{O}_\mathcal{N}, \mathcal{O}_\mathcal{S}, \mathcal{O}_\mathcal{E}, \mathcal{O}_\mathcal{W}$ on it, we generate a primitive state. Its elements are called parent states.
Primitive basis	States labeled by p, which form the basis pre-diagonalization in a certain iteration. Each primitive state has its own gender label, indicating its parent subspace.
Genders	Attribute of the primitive basis, indicating which parent state of the previous iteration generated it.
Invariants	Wigner–Eckart invariants of the parent states, required to construct off-diagonal matrix elements.

Source: By the author.

Number of states of each gender.
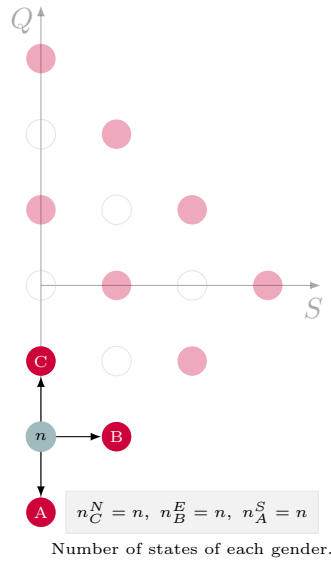
Figure 9 – Construction of the new basis in the checker-board representation. If the parent Subspace has n eigenstates, it generates n states of each gender in its neighbor subspaces.
Source: By the author.

gender $\mathcal{S}, \mathcal{W}, \mathcal{E}$, and $\mathcal{N}$. This becomes clear once we explain the actual construction of the Hamiltonian matrices.

The Hamiltonian operator, written in terms of a previous iteration, is

$$\mathcal{H}_N = \lambda \mathcal{H}_{N-1} + (f_{N-1}^\dagger f_N + H.c.). \tag{3.58}$$

To compute the diagonal matrix elements, we observe two things. First, the gender

operators, which define the new basis, are all unitary and commute with the first term on the left hand side. Therefore,

$$\mathcal{O}_g^\dagger \, H_{N-1} \, \mathcal{O}_g = H_{N-1}. \tag{3.59}$$

Second, the parent states do not contain any operators of site N. Hence, our only chance of having a non-vanishing second term on the left hand side is to combine the operators $\mathcal{O}_g^\dagger$ and $\mathcal{O}_g$ to destroy the site N operator. This is impossible for operators with the same gender, so that the second term always vanishes. Accordingly, they make no contributions to diagonal matrix elements, and we only need to look at the first term. Ultimately, the diagonal terms become

$$^g \langle q, s, s_z, p | \, \mathcal{H}_N \, | q, s, sz, p \rangle_N^g = \lambda E_{N-1}^{Q,S,Sz,\ell}, \tag{3.60}$$

where ℓ denotes its parent state. This is why it is essential to know its origin.

To compute the off-diagonal matrix elements, we must work in the same charge and spin subspace (by symmetry) and combine the genders. A general matrix element is

$$
\begin{aligned}
{}^{g'} \langle q, s, s_z, p' | H_A^N | q, s, s_z, p \rangle_N^g = &\sum_\mu \langle Q, S, S_z, \ell | \mathcal{O}_g^\dagger (f_{N-1\mu}^\dagger f_{N\mu}) \mathcal{O}_{g'} | Q', S', S_z', \ell' \rangle \\
&+ \langle Q, S, S_z, \ell | \mathcal{O}_g^\dagger (f_{N\mu}^\dagger f_{N-1\mu}) \mathcal{O}_{g'} | Q', S', S_z', \ell' \rangle .
\end{aligned}
\tag{3.61}
$$

On the left hand side, once again write the primitive basis in terms of its parent states. The off-diagonal operator is a hopping term between site N and $N-1$, while the operators $\mathcal{O}_g$ which generate the primitive basis, only have operators of the site N. This means the gender operators must necessarily differ from one creation/annihilation operator f_N. There can be no extra f_N operator in the matrix element, as they can not be compensated by choice of parent states (which do not contain the site N). The first term on the left hand side survives for the gender combinations $\{\mathcal{S}, \mathcal{E}\}$, $\{\mathcal{S}, \mathcal{W}\}$, $\{\mathcal{W}, \mathcal{N}\}$, $\{\mathcal{E}, \mathcal{N}\}$. The second term is non vanishing for $\{\mathcal{E}, \mathcal{S}\}$, $\{\mathcal{W}, \mathcal{S}\}$, $\{\mathcal{N}, \mathcal{W}\}$, $\{\mathcal{N}, \mathcal{E}\}$. By explicitly writing the gender operators and applying anticommutation relations, we obtain

$$
\begin{aligned}
{}^{g'} \langle q, s, s_z, p' | H_A^N | q, s, s_z, p \rangle_N^g = &\sum_\mu \alpha_{g'g}(S, S_z, \mu) \ \langle Q, S, S_z, \ell | f_{N-1\mu}^\dagger | Q', S', S_z', \ell' \rangle \\
&+ \alpha_{gg'}(S, S_z, \mu) \ \langle Q, S, S_z, \ell | f_{N-1\mu} | Q', S', S_z', \ell' \rangle .
\end{aligned}
\tag{3.62}
$$

The $\alpha_{g'g}(S, S_z, \mu)$ coefficients above are known: we can compute them with any gender combination. The most important thing to notice above is that, once again, the matrix element depends on a quantity that comes from the previous iteration. In this case, we need the matrix element of the parent states. For diagonal terms, we had their energy. Moreover, we can further simplify the equation by using that the Hamiltonian is rotationally invariant so that the Wigner-Eckart theorem applies. We can cast any matrix element as

$$\langle q, s', s_z' | f_\mu^\dagger | q, s, s_z \rangle = \langle q', s' || f^\dagger || q, s \rangle \left(\begin{array}{c|cc} S' & \frac{1}{2} & S \\ S_z' & \mu & S_z, \end{array} \right) \tag{3.63}$$

Table 3 – Non zero off diagonal matrix elements of the *Nth* iteration. Naturally, their conjugates do not vanish either, but they will not be used in our implementation.

g'	g	${}^{g'}\langle q, s, s_z, p'|H_A^N|q, s, s_z, p\rangle_N^g$
$\mathcal{E}$	$\mathcal{N}$	$\sqrt{\frac{2s}{2s+1}}\,\langle q, s-1/2, \ell'||f_{N-1}^\dagger||q-1, s, \ell\rangle_{N-1}$
$\mathcal{W}$	$\mathcal{N}$	$-\sqrt{\frac{2s+2}{2s+1}}\,\langle q, s+1/2, \ell'||f_{N-1}^\dagger||q-1, s, \ell\rangle_{N-1}$
$\mathcal{S}$	$\mathcal{E}$	$\langle q+1, s, \ell'||f_{N-1}^\dagger||q, s-1/2, \ell\rangle_{N-1}$
$\mathcal{S}$	$\mathcal{W}$	$\langle q+1, s, \ell'||f_{N-1}^\dagger||q, s+1/2, \ell\rangle_{N-1}$

Source: By the author
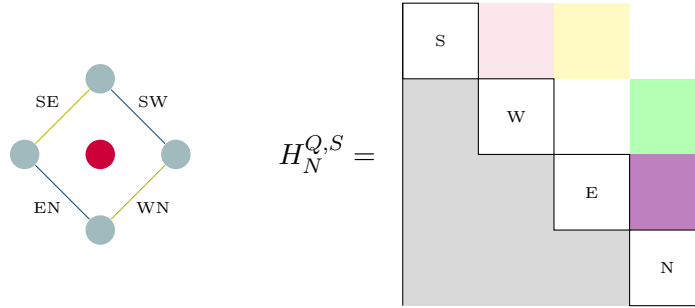
Figure 10 – Hamiltonian of subpace (Q, S) and iteration N, with its gender quadrants. The colored blocks are the non zero off-diagonal entries, and are called *sub-blocks*. On the left hand side, the central circle in red represents the subspace (Q, S, N), and the circles on the diamond shape are the parent subpaces (of the previous iteration). The sides of the diamond represent the invariants (Tab. 3), which are defined between two parent subspaces. The off-diagonal entries are proportional to them.
Source: By the author.

where the first bracket on the right-hand side is an *invariant*. Tab. 3 contains all non zero, non diagonal matrix elements, and Fig. 10 shows the structure of the final Hamiltonian. We order the primitive basis by gender, in $\mathcal{SWEN}$ order. As a consequence, we divide the non-diagonal elements in blocks linking two gender blocks, and we name them *sub-blocks*.

There are critical ingredients for an eNRG/NRG implementation. The first one is the energy of every subspace and iteration. They become the diagonal entries of subsequent iterations. They are also necessary to compute observables, as the many-body energies appear in Boltzmann factors. The next ingredient is the invariants of each iteration, required to compute future off-diagonal elements and matrix elements of interest, i.e., observables. Here, we will discuss how to calculate and store invariants. At last, we also

must discuss how to find matrix elements from invariants. We will cover these topics while explaining the code. Functions highlighted in pink are the main fucntions, while the ones in green are auxiliary functions.

Class `Subspace` will be present throughout the code. Each object from this class has three attributes:

- `eigblock`: Index of the parent subspace in the energy array of the previous iteration.

- `invariants`: Array with four entries $(\mathcal{SW}, \mathcal{SE}, \mathcal{EN}, \mathcal{WN})$. Each entry carries the position of the invariants in the invariants array. These are the same labels as Fig. 10.

- `gender`: Array with four entries $(n\mathcal{S}, n\mathcal{W}, n\mathcal{E}, n\mathcal{N})$. Each entry is the number of states with each gender forming the primitive basis.

Iterations will have their own Space matrix, such as in Fig. 11. The entries are the Subspace objects. This construction is useful for quickly accessing and organizing information such as energy and invariant indexes and dimensions of gender blocks (Fig. 10).
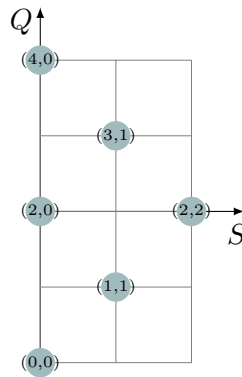

Figure 11 – Matriz $N = 0$.
Source: By the author.

We begin the first iteration $N = 0$ by calling the function `iteration_0`. It defines the initial Hamiltonian Eq. 3.49, diagonalizes it via `eig_blocks`, which implements the *ultra-violet cuttof*. The former function also fills the first space matrix, and the first invariant vector, which we computed analytically.

Fig. 12 shows how we fill the first invariants array and all other iterations will follow the same logic. Because they are matrix elements between parent states of neighboring subspaces, we represent invariants by the diagonal lines. There are two types of invariants: the ones in green pointing to the north-west and the ones in blue pointing to the east-west. The array has size six, corresponding to the six subspaces that can be kets. Following
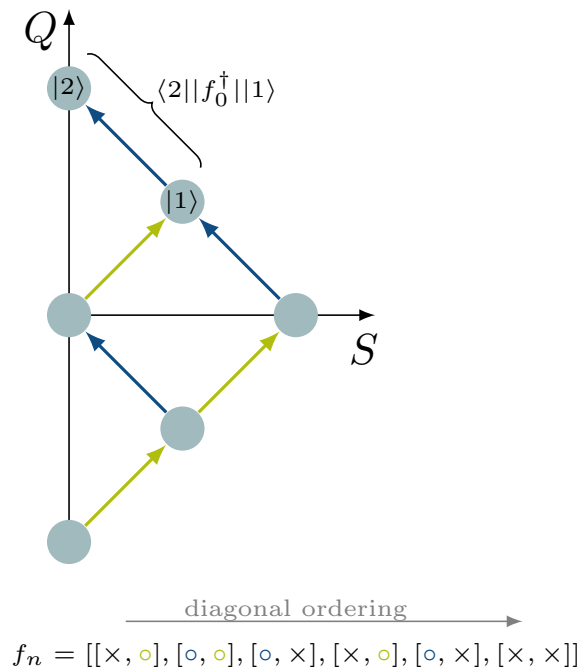
Figure 12 – Structure of the invariant array. It has six entries, for each subspace. The elements are vectors themselves: the first entry carrying invariant of the green kind, and the second entry of the blue kind. Only invariants where the subspace is a ket will be allocated in said subspace.
Source: By the author.

the diagonal ordering, we see the first subspace ($Q = -2, S = 0$) only has invariants of the green type. Next, ($Q = -1, S = 1/2$) has invariants of both types. Subspace ($Q = 0, S = 1$) has invariants of the green and blue kind, but its states are only kets in the blue line. Notice it would be redundant to allocate invariants where states are bras because these matrix elements would already have been allocated as kets of the previous subspace ($Q = -1, S = 1/2$). Accordingly, the last subspace has an empty entry because it cannot act as a ket.

At the end of iteration zero, we will have the first Space matrix, an array with the many-body energies of all subspaces (below *uv cutoff*), and the invariants array. The next step is calling the function `iteration_N`, which organizes all required steps in one subroutine. First, we must create the new Space matrix with `new_Space`, which will facilitate the Hamiltonian construction. It generates an empty Space matrix via `empty_Space`, large enough to accommodate the checker-board structure of the current iteration (as in Fig. 11). Function `around_Descendants` fills the subspace objects. It receives a subspace of `Space0` (parent states), with child states in `Space`. The purpose is to keep track of

- the index of the parent energies in the energy array, of the previous iteration;

- the number of child states of each gender subspace (Q, S) creates in the four cardinal directions;

- the position of the relevant invariants in the invariants array.

Fig. 13 expands the explanation on the last item. The subspace in blue belongs to `Space0` and is fed into our function. There is only one entry of the invariants array associated with it: the first one. However, by comparison to Fig. 10, we see that the same invariant enters the sub-block $\mathcal{WN}$ for a state in C and sub-block $\mathcal{SE}$ for a state in B.
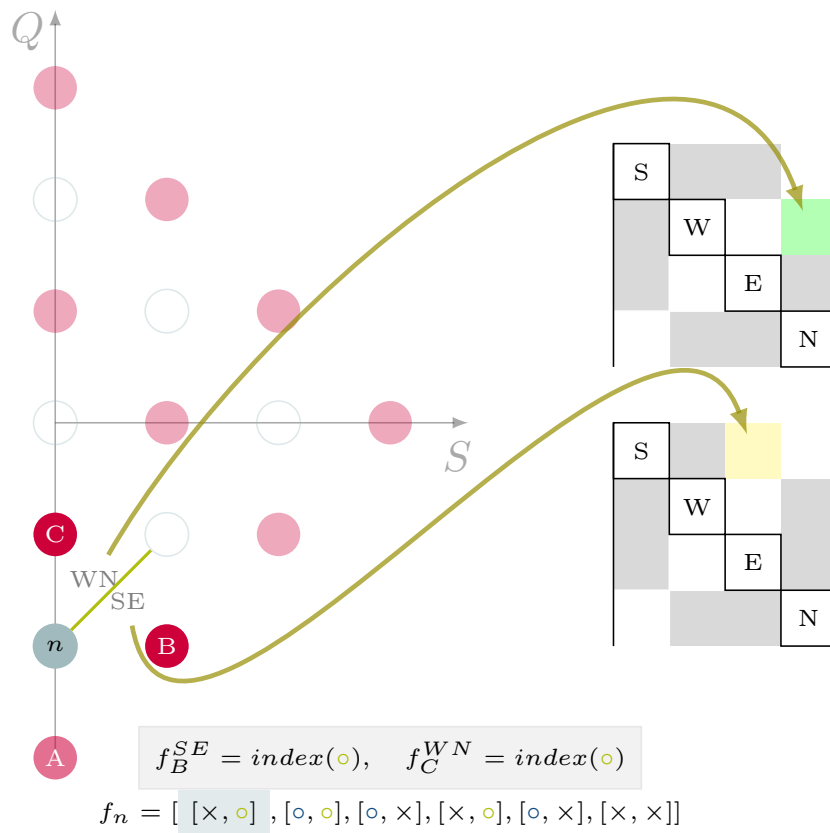
Figure 13 – As shown in Fig. 10, the same invariant contributes to two distinct off-diagonal blocks in the primitive Hamiltonian. For C, the contribution is to the non-diagonal sub-block $\mathcal{WN}$, while for B, the contribution is to $\mathcal{SE}$. The parent subspace does not fill the invariants of the child to south because we are only interested in invariants where the parent state is the ket.
Source: By the author.

With the information provided by `Space` in hands, we construct the new Hamiltonian with function $\boxed{\text{HN}}$ and organize the basis states by gender in blocks of order $\mathcal{SWEN}$. The construction of the diagonal part is trivial because the attribute `eigblock` of each subspace is an array with four entries, which are the indexes we need to access

the energies of the parents of $\mathcal{SWEN}$. Next, we deal with the off-diagonal part via the function `fills_NonDiagonal`. Here, we know the size of the off-diagonal sub-blocks and the relevant invariants because of the attributes `gender` and `invariants` of `Space`, respectively. The Hamiltonian is then diagonalized by `eig_blocks`, where E_{uv}, the cutoff energy, must be manually changed inside this function.

The last step in every iteration is computing its invariants via `invariants`. We followed the approach detailed in Pinto and Oliveira, Sec. *A.4.3. Computation of invariants.* [17] The authors show how to reduce this calculation to multiplications of unitary change of basis matrices (between primitive and parent states) and tabulated coefficients. Despite its simple implementation, this function is the bottleneck of any eNRG/NRG code due to the many matrix multiplications. Although the vital part of our code is in Python language, this specific function is a Fortran extension to increase performance. Finally, function `matrix_elements` recursively computes the matrix elements of the first bath and impurity sites as they are necessary to find thermoelectric properties. This recursive calculation is the main topic of Pinto and Oliveira. [17]

<div style="background-color: #3a3a5e; color: white;">4</div>

Thermoelectric properties and Universality

Universality studies in the Anderson model are almost as old as the NRG method itself.[14] As Wilson's creation was employed to describe new physical quantities, universality was often discussed, and currently, contributions are still reported. These studies are relevant because they provide theoretical expectations for results with different model parameters. They reduce the temperature dependence to universal curves calculated at the symmetric point and deal with asymmetry via parameter-dependent constants. Furthermore, they are especially pertinent as nanodevice experiments advance because they provide simple ways to verify experimental results and offer evidence of Kondo physics. In this section, we study universality concepts along the same lines as Yoshida *et al.*, while extending the discussion to the energy moments $\mathcal{L}_1(T)$ and $\mathcal{L}_2(T)$.[15]

4.1 Energy moments

In this work, we employed eNRG to investigate the thermoelectric properties of a SCD. They were computed from the energy moments

$$\mathcal{L}_n \equiv \frac{2}{h} \int \left(-\frac{\partial f}{\partial \epsilon}\right) (\beta\epsilon)^n \rho(\epsilon, T) d\epsilon, \tag{4.1}$$

where $f(\epsilon)$ is the Fermi function, $\beta \equiv 1/(k_B T)$ is the reciprocal of the thermodynamic temperature and the spectral density of the a_0 orbital is

$$\rho(\epsilon, T) = \frac{1}{\mathcal{Z} f(\epsilon)} \sum_{m,n,\sigma} e^{-\beta E_n} |\langle m| a_{0,\sigma} |n\rangle|^2 \delta(\epsilon + E_m - E_n). \tag{4.2}$$

Here, $|m\rangle$ ($|n\rangle$) is an eigenstate of a certain Hamiltonian with eigenvalue E_n (E_m) and $\mathcal{Z}(T)$ is the partition function.

Combinations of energy moments yield the electric conductance G, thermopower S, and thermal conductance κ, respectively [22,23]:

$$G(T) = e^2 \mathcal{L}_0(T) \tag{4.3}$$

$$S(T) = -\frac{\mathcal{L}_1(T)}{e\mathcal{L}_0(T)}; \tag{4.4}$$

$$\beta\kappa(T) = \mathcal{L}_2(T) - \frac{\mathcal{L}_1^2(T)}{\mathcal{L}_0(T)}. \tag{4.5}$$

We only have to compute the three energy moments to determine the transport properties. Therefore, we obtain them from eigenvalues and matrix elements of the operator a_0, both byproducts of iterative diagonalization. Further, we evaluate the matrix elements recursively using the faster and less demanding method presented in reference. [17]

4.2   Fixed point Hamiltonians

In this section, the role of the fixed points of the RG transformation will become apparent. As we add more sites to the Wilson chain, we renormalize the Hamiltonian. After each iteration, we obtain a renormalized energy spectrum. This spectrum will remain the same within an iteration window when we are at a fixed point. Around these points, we describe the Anderson Hamiltonian by a simple fixed-point Hamiltonian plus corrections, which determine their stability. In the Kondo regime, there are two fixed points - the Local Moment (LM) and the frozen Level - linked by a crossover region. Unlike the transition from the Free Orbital (FO) fixed point to one of the LM fixed points, the LM-FL crossover is universal. As a consequence, the thermodynamical properties of the Kondo regime are universal functions of temperature divided by the Kondo temperature.[24]

The effects of universality on temperature-dependent transport properties are more subtle. We understand this statement via scattering theory, which tells us that a model with a phase shift δ had a probability $\cos^2(\delta)$ of transmission across the SCD. Therefore, because the phase-shift is parameter dependent, so are the transport properties, and they can not be universal. However, in line with the results, we will show that one can still profit from the universal crossover when analyzing these properties.[21] Moreover, we notice that universality studies are not valid beyond the Kondo regime, where only pure eNRG computations are reliable.

The LM and the FL are depicted by the side arrows in Fig. 2. Around the LM, thermal or excitation energies are higher than the energy width defined by the Kondo temperature Γ_K, and the impurity is not screened. As a consequence, this fixed-point describes a conduction band with a free spin. By decreasing the temperature, the Hamiltonian moves away from the LM instability and towards the FL. For temperatures much lower than the Kondo temperature, the impurity is completely screened. At the FL

fixed point, sites d and a_0 are so strongly coupled (singlet) that they decouple from the bath, and a conduction band also describes the physics.

The fixed-point Hamiltonians are, in k-space,

$$H^*_{LM} = \sum_{k,\sigma} \epsilon_k a^\dagger_{k,\sigma} a_{k,\sigma} + W_{LM} \sum_\sigma a^\dagger_{0,\sigma} a_{0,\sigma}, \tag{4.6}$$

and

$$H^*_{FL} = \sum_{k,\sigma} \epsilon_k a^\dagger_{k,\sigma} a_{k,\sigma} + W_{FL} \sum_\sigma a^\dagger_{0,\sigma} a_{0,\sigma}, \tag{4.7}$$

where the last terms on the left hand sides are parameter dependent scattering potentials applied to the first site, usually found by NRG computations. Both Hamiltonians can be cast in diagonal form, which we show in appendix A.3. They become

$$H^*_{LM} = \sum_{k,\sigma} \varepsilon_k g^\dagger_{k,\sigma} g_{k,\sigma}, \tag{4.8}$$

and

$$H^*_{FL} = \sum_{k,\sigma} \tilde{\varepsilon}_k \tilde{g}^\dagger_{k,\sigma} \tilde{g}_{k,\sigma}, \tag{4.9}$$

with phase-shifted energies

$$\varepsilon_k = \epsilon_k - \frac{\delta_{LM}}{\pi} \Delta \tag{4.10}$$

and

$$\tilde{\varepsilon}_k = \epsilon_k - \frac{\delta}{\pi} \Delta. \tag{4.11}$$

The energies are uniformly shifted. In particular, the LM phase-shift is

$$\tan(\delta_{LM}) = -\pi \rho W_{LM}, \tag{4.12}$$

and it relates to the FL phase-shift via the Friedel-Sum rule[25]

$$\delta = \delta_{LM} + \frac{\pi}{2}. \tag{4.13}$$

In the symmetric point, particle-hole symmetry determines that $W_{LM} = 0$, which implies that $\delta_{LM} = 0$ and that $\delta = \pi/2$.

4.3 Universal matrix elements

In the Kondo Regime, the Schrieffer-Wolff transformation proves that the Anderson and Kondo model are equivalent.[26] Therefore, in this parametric regime, the Anderson model becomes

$$H_J = \sum_{k,\sigma} \epsilon_k a^\dagger_{k,\sigma} a_{k,\sigma} + W_{LM} \sum_\sigma a^\dagger_{0,\sigma} a_{0,\sigma} + J \sum_{\mu\nu} a^\dagger_{0\mu} \sigma_{\mu\nu} a_{0\nu} \cdot \mathbf{S}, \tag{4.14}$$

where

$$J = \frac{2V^2 U}{|V_g|(V_g + U)} \tag{4.15}$$

We cast the Hamiltonian H_J in a form with no scattering potential by changing its basis to the eigenstates of the Local-Moment fixed point Hamiltonian, namely,

$$H_J = \sum_{\ell,\sigma} \varepsilon_\ell g^\dagger_{\ell,\sigma} g_{\ell,\sigma} + J_W \sum_{\mu\nu} \phi^\dagger_{0\mu} \sigma_{\mu\nu} \phi_{0\nu} \cdot \mathbf{S} \tag{4.16}$$

where

$$\phi_{0,\sigma} = \frac{1}{\sqrt{N}} \sum_\ell g_{\ell,\sigma}, \tag{4.17}$$

and

$$J_W = J \cos^2(\delta_{LM}) \tag{4.18}$$

Although the Hamiltonians Eqs. 4.14, and 4.16 describe the same physical process, the latter reveals universality. Eq 4.16 is formed by a fixed point Hamiltonian and one operator that drives the system from one fixed point to another, even for the particle-hole asymmetric case $W_{LM} \neq 0$. When the system evolves from the LM to the FL, the eigenvalues of H_J scale with T_K. Any two sets of parameters in the Kondo regime have eigenvalues and eigenvectors being each other scaling images. Concretely, this means that the same eigenstates appear in the trajectory between fixed points, but in different temperatures, governed by T_K. Furthermore, matrix elements of the fixed point eigenoperators g_ℓ are also universal, and so are their linear combinations. We formulate our universality study in terms of the universal matrix elements $\langle m| \phi_0 |n\rangle$ and $\langle m| \phi_1 |n\rangle$, where

$$\phi_{1,\sigma} = \sqrt{\frac{\lambda^2 - 1}{2\lambda}} \sum_\ell \frac{\varepsilon_\ell}{D} \, g_{\ell,\sigma} \tag{4.19}$$

.

The energy moments, Eq. 4.1, are not calculated with the universal matrix elements $\langle m|\phi_0|n\rangle$ and $\langle m|\phi_1|n\rangle$. Instead, they are computed with the matrix elements $\langle m|a_0|n\rangle$, which are universal exclusively in the symmetric point, where $a_0 = \phi_0$. Naturally, universality studies for the asymmetric case require writing these matrix elements in terms of the universal ones. Appendix A.4 shows that this is simply

$$\langle m|a^\dagger_{0,\sigma}|n\rangle = \alpha_0 \langle m|\phi^\dagger_{0,\sigma}|n\rangle + \alpha_1 \langle m|\phi^\dagger_{1,\sigma}|n\rangle \,, \tag{4.20}$$

where α_0 and α_1 are model-parameters dependent constants. The constants and matrix elements can be assumed real with no loss of generality, as the truncated Hamiltonian has only real entries.

In order to reevaluate the energy moments in terms of the universal matrix elements, we rewrite the spectral density, Eq. 4.2, by mens of Eq. 4.20, yielding

$$\rho(\epsilon, T) = \alpha_0^2 \, \rho_0(\epsilon, T) + \alpha_1^2 \, \rho_1(\epsilon, T) + \alpha_0 \alpha_1 \, \rho_{01}(\epsilon, T), \tag{4.21}$$

where

$$\rho_{ii}(\epsilon, T) = \sum_{mn,\sigma} \frac{e^{-\beta E_n}}{\mathcal{Z} f(\epsilon)} |\langle m| \, \phi_{i,\sigma} \, |n\rangle|^2 \delta(\epsilon + E_m - E_n), \tag{4.22}$$

$i = 0, 1$, and

$$\rho_{01}(\epsilon, T) = \sum_{mn,\sigma} \frac{e^{-\beta E_n}}{\mathcal{Z} f(\epsilon)} (\langle m| \, \phi_{0,\sigma} \, |n\rangle \, \langle n| \, \phi_{1,\sigma}^\dagger \, |m\rangle + c.c.)$$
$$\delta(\epsilon + E_m - E_n). \tag{4.23}$$

All functions on the right hand side of 4.21 are universal in the Kondo regime. Accordingly, so are the energy moments

$$\mathcal{L}_j(T) = \alpha_0^2 \mathcal{L}_{00}^{(j)}(T) + \alpha_1^2 \mathcal{L}_{11}^{(j)}(T) + \alpha_0 \alpha_1 \mathcal{L}_{01}^{(j)}(T), \tag{4.24}$$

where

$$\mathcal{L}_{ii'}^{(j)} = \frac{2}{h} \int \left(-\frac{\partial f}{\partial \epsilon} \right) (\beta \epsilon)^j \rho_{ii'}(\epsilon, T) \, d\epsilon, \tag{4.25}$$

with $j = 0, 1, 2$. As a result, any set of parameters in the Kondo regime suffice to compute the right hand side functions of Eq. 4.24. However, symmetry considerations can simplify the problem. In the symmetric point, every positive energy has a negative equivalent. Hence, when $\epsilon \to -\epsilon$ in the spectral densities, everything but ϕ_1, which is proportional to ϵ, remains the same. Thus, $\rho_{01}(\epsilon, T)$ is an odd function and $\rho_i(\epsilon, T)$ $(i = 0, 1)$ are even functions. Because the integrals 4.25 have symmetric limits,

$$\mathcal{L}_{01}^{(0)} = \mathcal{L}_{01}^{(2)} = \mathcal{L}_{00}^{(1)} = \mathcal{L}_{11}^{(1)} = 0, \tag{4.26}$$

which leads to the much simpler expressions

$$\mathcal{L}_0(T) = \alpha_0^2 \mathcal{L}_{00}^{(0)}(T) + \alpha_1^2 \mathcal{L}_{00}^{(1)}(T), \tag{4.27}$$

$$\mathcal{L}_1(T) = \alpha_0 \alpha_1 \mathcal{L}_{01}^{(1)}(T), \tag{4.28}$$

and

$$\mathcal{L}_2(T) = \alpha_0^2 \mathcal{L}_{00}^{(2)}(T) + \alpha_1^2 \mathcal{L}_{11}^{(2)}(T). \tag{4.29}$$

4.4   Universal mapping

The universal functions $\mathcal{L}_{00}^{(0)}(T)$ and $\mathcal{L}_{00}^{(2)}(T)$ are the symmetric point energy moments ($\mathcal{L}_0^S(T)$, $\mathcal{L}_2^S(T)$), since $a_0 = \phi_0$ in this case. Hence, by writing the spectral function

$\rho_{11}(\epsilon, T)$ in terms of $\rho_{00}(\epsilon, T)$, we can reduce all temperature dependence in Eqs. 4.27 and 4.29 to the familiar symmetric point energy moments. This is done in Appendix A.5, and yields, for all $k_B T \ll D$,

$$\rho_{11}(\epsilon, T) = \frac{2}{\pi^2} \ (\rho - \rho_{00}(\epsilon, T)), \tag{4.30}$$

where ρ is the density of conduction states per particle and per spin.

Substitution on the right hand side of Eqs. 4.27 and 4.29 shows that all energy moments are linearly mapped onto universal functions, i.e,

$$\mathcal{L}_0(T) = \left(\alpha_0^2 - \tilde{\alpha}_1^2\right) \mathcal{L}_0^S(T) + \frac{2}{h}\tilde{\alpha}_1^2, \tag{4.31}$$

$$\mathcal{L}_1(T) = \alpha_0 \alpha_1 \mathcal{L}_1^{01}(T), \tag{4.32}$$

and

$$\mathcal{L}_2(T) = \left(\alpha_0^2 - \tilde{\alpha}_1^2\right) \mathcal{L}_2^S(T) + \frac{2}{h}\frac{\pi^2}{3}\tilde{\alpha}_1^2, \tag{4.33}$$

where $\tilde{\alpha}_1 \equiv \sqrt{2}\alpha_1/\pi$. Then, the last step in the universality formulation is determining the coefficients α_0 and α_1.

4.4.0.1 Parameter dependent constants

The behavior of the first energetic moment for the symmetric Anderson Hamiltonian is a well-known result. [21] With its high and low-temperature values, along with the fixed point energy moments, we determine the parameter-dependent constants α_0 and α_1. At the Frozen Level fixed point, $\mathcal{L}_0^S = 0$. The comparison between Eq. 4.31 and Eq. A.68 then yields

$$\alpha_0^2 = \sin^2(\delta). \tag{4.34}$$

Likewise, at the Local Moment fixed point, $\mathcal{L}_0^S = 2/h$, which results, by comparison with Eq. A.69, in

$$\tilde{\alpha}_1^2 = \cos^2(\delta). \tag{4.35}$$

In terms of the phase-shifts and in units of $2\rho/h$, the linear mappings Eqs. 4.31, 4.32, and 4.33 take the much simpler form

$$\mathcal{L}_0(T/T_K) = -\cos(2\delta) \ \mathcal{L}_0^S(T/T_K) + \frac{1}{h}(1 + \cos(\delta)), \tag{4.36}$$

$$\mathcal{L}_1(T/T_K) = \frac{\pi}{\sqrt{2}}\sin(2\delta)\mathcal{L}_{01}^{(1)}(T/T_K), \tag{4.37}$$

and

$$\mathcal{L}_2(T/T_{\mathrm{K}}) = -\cos(2\delta)\,\mathcal{L}_2^S(T/T_{\mathrm{K}}) + \frac{\pi^2}{3h}(1 + \cos(\delta)). \tag{4.38}$$

The expressions above are the final form of the universal linear mapping of the energy moments. They reduce all temperature dependence to the universal functions, which we need to compute only once. At the particle-hole symmetric point $\delta = \pi/2$, and, as expected, $\mathcal{L}_0$ and $\mathcal{L}_2$ are the universal functions. The function $\mathcal{L}_1$ also has a special behavior at this point: it is identically zero. The particle-hole asymmetry description lies in the phase shifts. It makes $\mathcal{L}_1$ nonvanishing and flattens the temperature dependence of $\mathcal{L}_1$ and $\mathcal{L}_2$. The most accurate method for their estimate requires the many-body energy spectrum, calculated with eNRG or NRG , and is described by Yoshida *et al.* [15]

Numerical Results

This section contains universality and eNRG results for the runs in Tab. 4. In Sec 5.1, we analyze the conductance, thermopower, and thermal conductance. Runs A-C belong to the Kondo regime through the whole shown temperature range. Runs a-c have deviations at high temperatures. In the Kondo regime, universality considerations are valid, and we examine them in section 5.2, yielding a theoretical prediction to the Wiedmann-Franz law in Sec. 5.3, and for the figure of merit in Sec. 5.4.

5.1   Themoelectric properties

Table 4 shows the eNRG runs that we examined and their representative colors. Fig. 14 shows the numerical results for conductance, thermopower, and thermal conductance as functions of temperature scaled by the Kondo temperature.

The first $(G(T/T_K))$ and third $(\beta\kappa(T/T_K))$ quantities have a similar temperature and gate potential dependence. They both increase monotonically from zero to a saturation value, with overlaying lines for distinct values of V_g. The maximum value of the conductance

Table 4 – Model parameters, phase shifts and Kondo temperatures for the eNRG runs analysed throughout section 5.

Run	Symbol	U	V_g/U	δ/π	$k_B T_K/t$
a	——	0.01	$-0.5.$	0.500	6.4×10^{-5}
b	········	0.01	-0.65	0.491	1.5×10^{-4}
c	- - - -	0.01	-0.80	0.470	2.0×10^{-3}
A	——	10	$-0.5.$	0.500	6.4×10^{-5}
B	········	10	-0.65	0.491	1.5×10^{-4}
C	- - - -	10	-0.80	0.470	2.0×10^{-3}

Source: By the author.

is unity, and the thermal conductance is $\pi^2/3$. The parameters of runs a-c lie within the Kondo regime for all temperatures depicted, and the phase shifts are all very close to $\pi/2$. All we can see in the figure is the Kondo crossover. As the temperature decreases, the Kondo cloud begins to form, and the strengthened coupling between conduction states and impurity hinders conduction.

The overlap in the first and last panels is no coincidence: it is a consequence of universality in the Kondo regime. Proportional to $\mathcal{L}_0(T/T_\mathrm{K})$, the conductance is linearly mapped onto the universal function $\mathcal{L}_{00}^{(0)}(T/T_\mathrm{K})$ via Eq. 4.36. The linear and angular coefficients are $\cos(2\delta)$ functions and are very close to one another for all runs, as the phase shifts are close to each other. Hence, the conductance curves coincide. We can devise a similar argument for the thermal conductance, with one complication: this property is not proportional to an energetic moment. It has a more complex dependence — nevertheless, the second term in Eq. 4.5 is only a minor correction to the function $\mathcal{L}_2(T/T_\mathrm{K})$, which is linearly mapped onto the universal function $\mathcal{L}_{00}^{(2)}(T/T_\mathrm{K})$.

In contrast, the thermopower ($S(T/T_K)$) has significantly distinct curves, with a minimum increasing in temperature as we increase the gate potential. It is noteworthy that this quantity is negative for all chosen gate potentials, except at the symmetric point, where it vanishes. When the gate potential is $V_g > U/2$, the thermopower becomes positive. Hence, unlike the conductance and thermal conductance, the thermopower is very sensitive to particle-hole asymmetry.

Runs a-c (Fig. 15) have a much smaller interaction $U = 0.01D$, such that for $T > 10T_\mathrm{K}$, the system is no longer in the Kondo regime. By comparing Figs. 14 and 15 we see the non-universal behavior in the new and broad peaks (conductance and thermal conductance) and valley (thermopower), corresponding to the cross-over from free-orbital to local-moment fixed points. For $T < 10T_\mathrm{K}$, we again have the Kondo crossover, and the first and last panels have overlapping curves.

5.2 Universal curves

As explored in section 4, the energy moments display universality in the Kondo regime. Therefore, Eqs. 4.27, 4.28, and 4.29 map these functions computed out of the symmetric point onto universal functions. Accordingly, these are independent of the parameters, and we must evaluate them only once. Fig. 16 shows the universal energy moments for $j = 0, 1, 2$. We chose to work with $\mathcal{L}_{01}^{(1)}(T/T_K)$ since the proportional function $\mathcal{L}_1(T/T_K)$ cancels in the symmetric point, due to particle-hole symmetry.
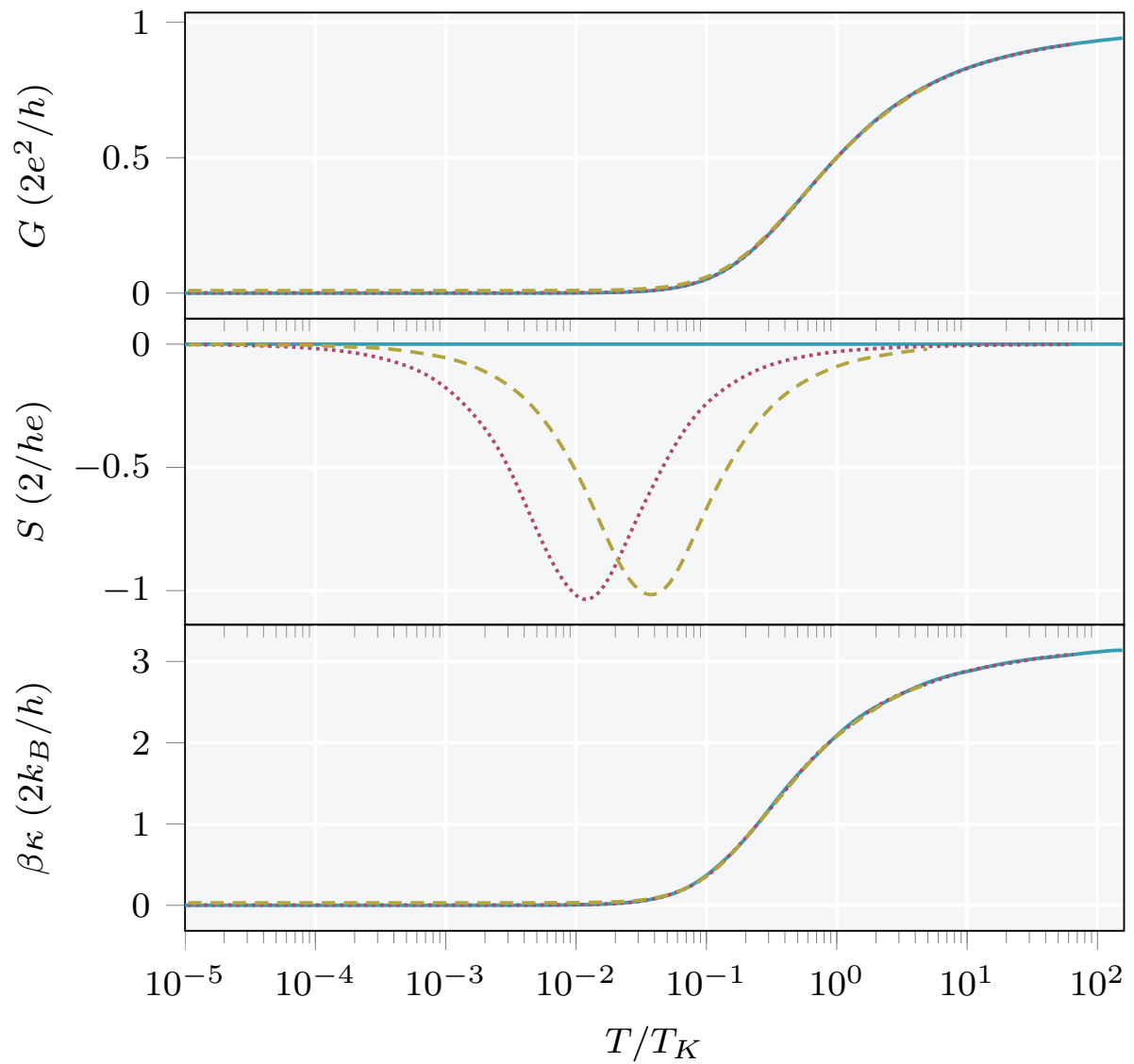
Figure 14 – Temperature dependences of conductance, thermopower, and thermal conductance. All quantities are computed from Eqs. 4.3, 4.4, and 4.5, for runs A-C. Only the thermopower is markedly affected by particle-hole asymmetry. Source: By the author.
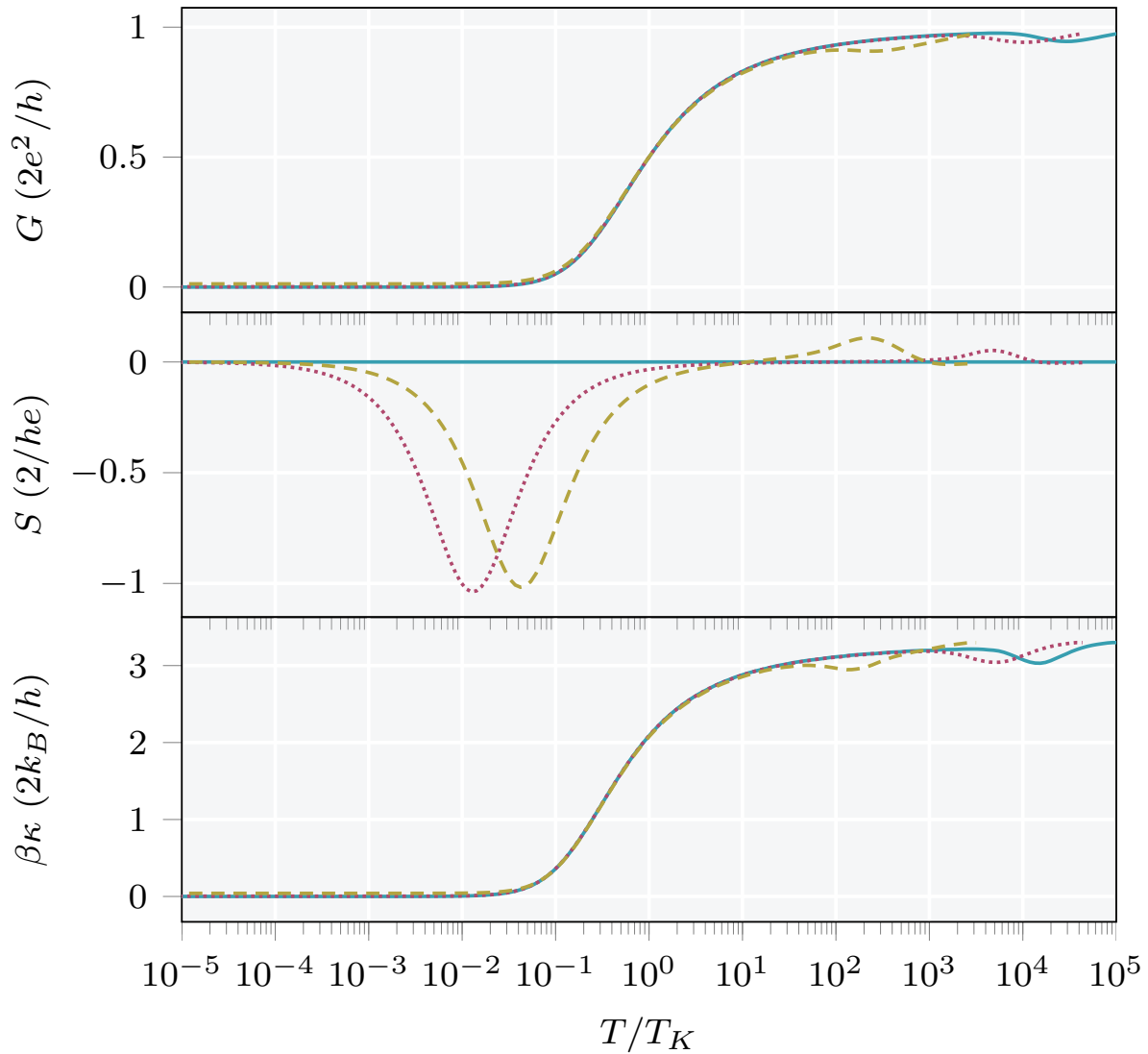
Figure 15 – Temperature dependences of conductance, thermopower, and thermal conductance as functions of temperature scaled by T_K. All quantities are computed from Eqs. 4.3, 4.4, and 4.5, for runs A-C. There are two crossovers in each pannel. The first one, from the FO to the LM, takes place for $T > T_K$, and is not universal. For lower temperatures, we have the universal Kondo crossover from the LM to the FL.
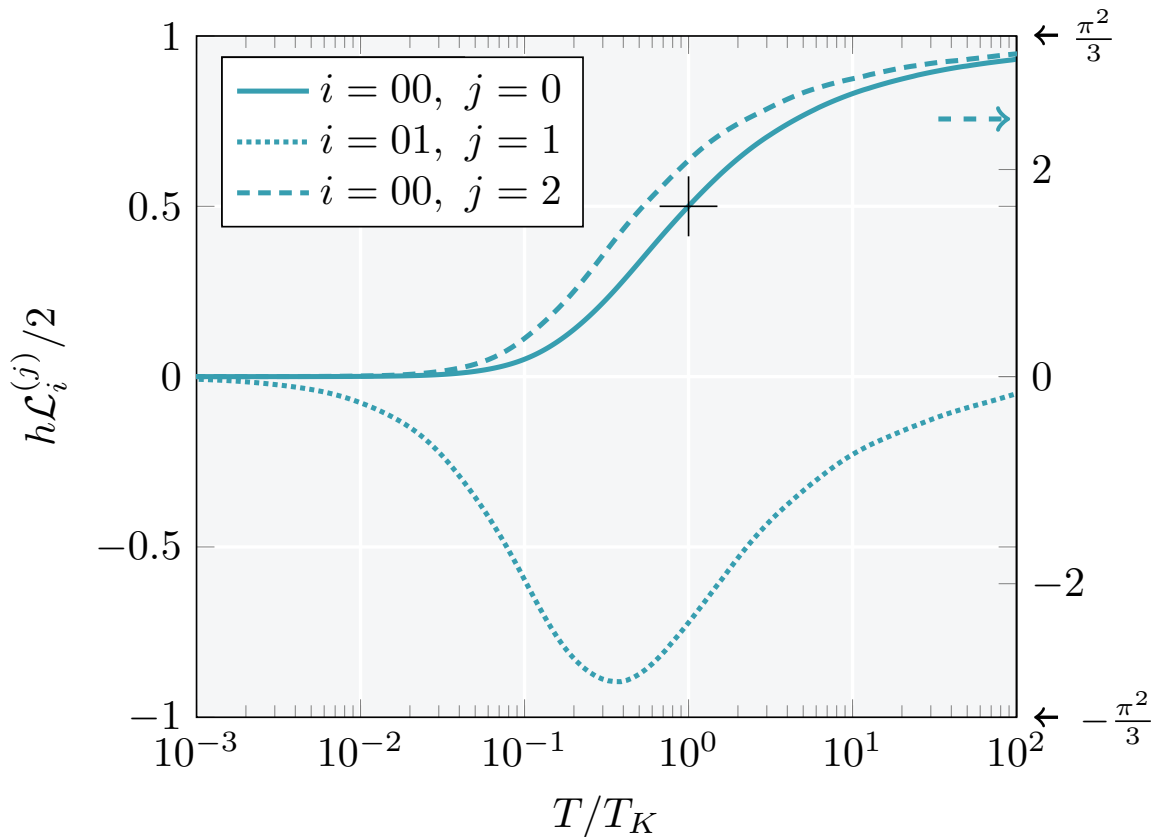Source: By the author.

Figure 16 – Universal energy moments $\mathcal{L}_{00}^{(0)}$, $\mathcal{L}_{01}^{(1)}$, $\mathcal{L}_{00}^{(2)}$ as functions of the temperature scaled by the Kondo temperature. The hairlines mark the point where $h\mathcal{L}_{00}^{(0)}/2 = 0.5$, which defines the Kondo temperature.
Source: By the author.

The energetic moment $j = 0$ (solid line) is proportional to the conductance in the Kondo regime, at the symmetric point. It monotonically grows, from zero to unity, going through the Kondo temperature at $\mathcal{L}_0^S(T/T_K) = 0.5$, which defines this temperature, marked by the hairlines. Function $j = 2$ (dashed line) has a similar form, with a maximum value $\mathcal{L}_2^S(T/T_K) = \pi^2/3$. In contrast, curve $j = 1$ (dotted line) exhibits a minimum value before the Kondo temperature, centered at $T \approx 0.4T_\mathrm{K}$.

For runs A-C in Table 4, Fig. 17a shows $\mathcal{L}_0(T/T_K)$ as a function of temperature scaled by the Kondo temperature. The filled circles from the eNRG runs are in excellent agreement with the solid lines, which originate from the universal mapping and are parametrized by the tabulated phase-shifts δ. Fig. 17b shows the same energy moments as a function of the universal curve $\mathcal{L}_{00}^{(0)}(T/T_k)$. As expected, the mapping is linear, and deviations from the solid lines are insignificant at this scale.

On the other hand, deviations become noticeable in Fig. 18, since they are the same scale as $\mathcal{L}_1(T/T_K)$. Predictably, the plot and its inset show this energetic moment to
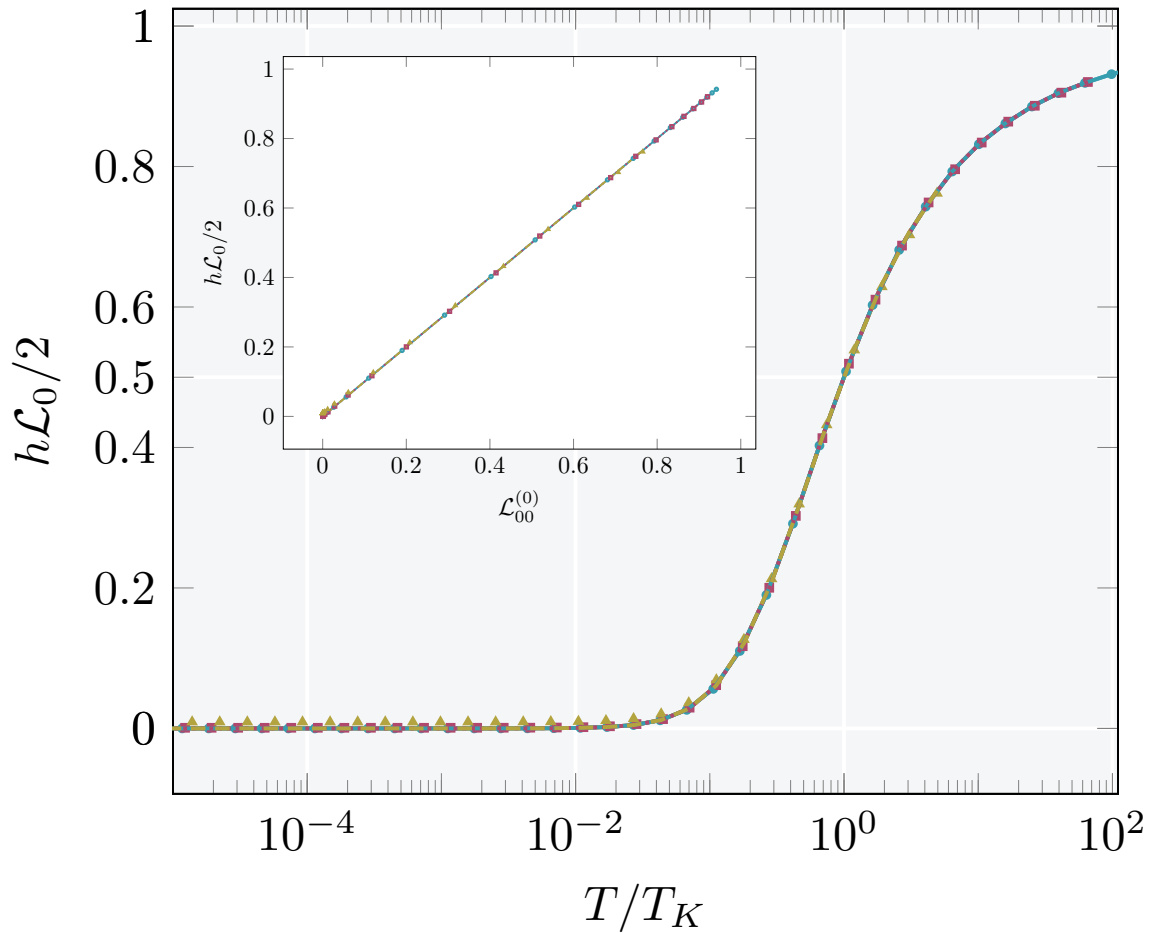
Figure 17 – First energetic moment as a function of temperature scaled by T_{K}. The scattered points are numerical results of the eNRG runs A-C in Table 4, and the solid lines originate from Eq. 4.36, parametrized by the phase shifts. The lines in the main plot overlap since this quantity is relatively indifferent to particle-hole asymmetry.The inset shows the energetic moment as a function of the universal curve $\mathcal{L}_{00}^{(0)}(T/T_K)$. The mapping is linear and is in very good agreement with the solid lines.

Source: By the author.

vanish at the symmetric point, which signals the transition between positive and negative functions. Because all gate potential values are such that $V_g + U/2 < 0$, all shown functions are positive. There is a manifest difference between the plots: this quantity is quite sensitive to particle-hole asymmetry. As a consequence, so is the thermopower.

The inset in Fig 18 shows eNRG markers adjusting well to the universal line; nevertheless, we see slight deviations for the magenta squares at $T \gtrsim 5T_{\mathrm{K}}$, and large deviations for the olive triangles. The reason behind them is that we are exiting the Kondo regime. As we move further away from the symmetric point, the high-temperature adjustment worsens, which happens because the Kondo temperature is high, and thermal excitations are no longer much smaller than the bandwidth. As a consequence the parameters no longer obey Eq. 2.10, and universality considerations are less precise. Here, contributions from the $\mathcal{O}(\rho k_{\mathrm{B}} T)$ terms become relevant, which were neglected in Eq. 18.

It is possible to analyze $\mathcal{L}_2(T/T_K)$ in analogy to $\mathcal{L}_0(T/T_K)$. This energetic moment, Fig. 19, does not significantly change for the various gate potentials, and neither does the thermal conductance. Although Eq. 4.5 also includes the sensitive $\mathcal{L}_1(T/T_K)$, $\mathcal{L}_2(T/T_K)$ is two orders of magnitude greater. Hence, only the thermopower is markedly affected by particle-hole asymmetry.

5.3   The Wiedemann-Franz law

The Wiedemann-Franz law states that the ratio of electronic thermal conductivity and electric conductivity is

$$\frac{\kappa(T)}{G(T)} = L_0 T, \tag{5.1}$$

where the constant $L_0 = \pi^2/3[k_B/e]$ is the Lorenz number. This law is famously obeyed both in the high and very low-temperature regimes, constituting a triumph of the free-electron theory. In our study, these regimes are Fermi-liquid fixed points that we called Local Moment and Frozen Level. At these fixed points, the energy moments are (Eqs. 4.36 and 4.38)

$$\mathcal{L}_0^{\mathrm{LM}} = \frac{2}{h}\sin^2(\delta),$$

$$\tag{5.2}$$

$$\mathcal{L}_2^{\mathrm{LM}} = \frac{2\pi^2}{3h}\sin^2(\delta),$$
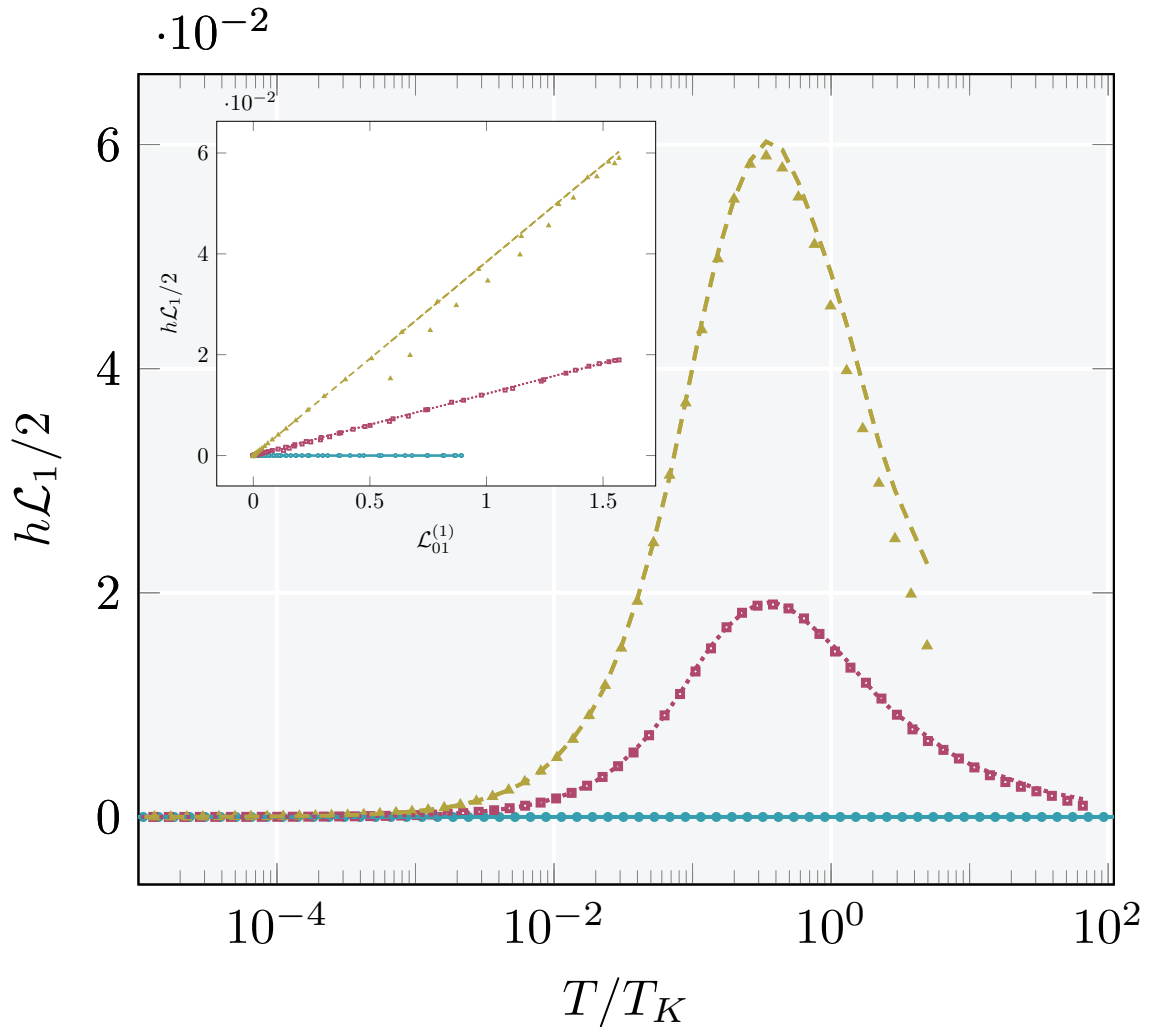
Figure 18 – Second energetic moment as a function of temperature scaled by T_{K}. It characterizes the thermopower and contributes to the thermal conductance. All markers are numerically computed from eNRG runs A-C. While the markers agree well with the solid lines for $T \lesssim T_{\mathrm{K}}$, there are clear deviations for higher temperatures. The inset shows this energetic moment as a function of the universal curve $\mathcal{L}_{01}^{(1)}(T/T_K)$. The mapping is linear, as anticipated by Eq. 4.37; nevertheless, the high temperature points still deviate from the solid line, as we exit the Kondo regime.
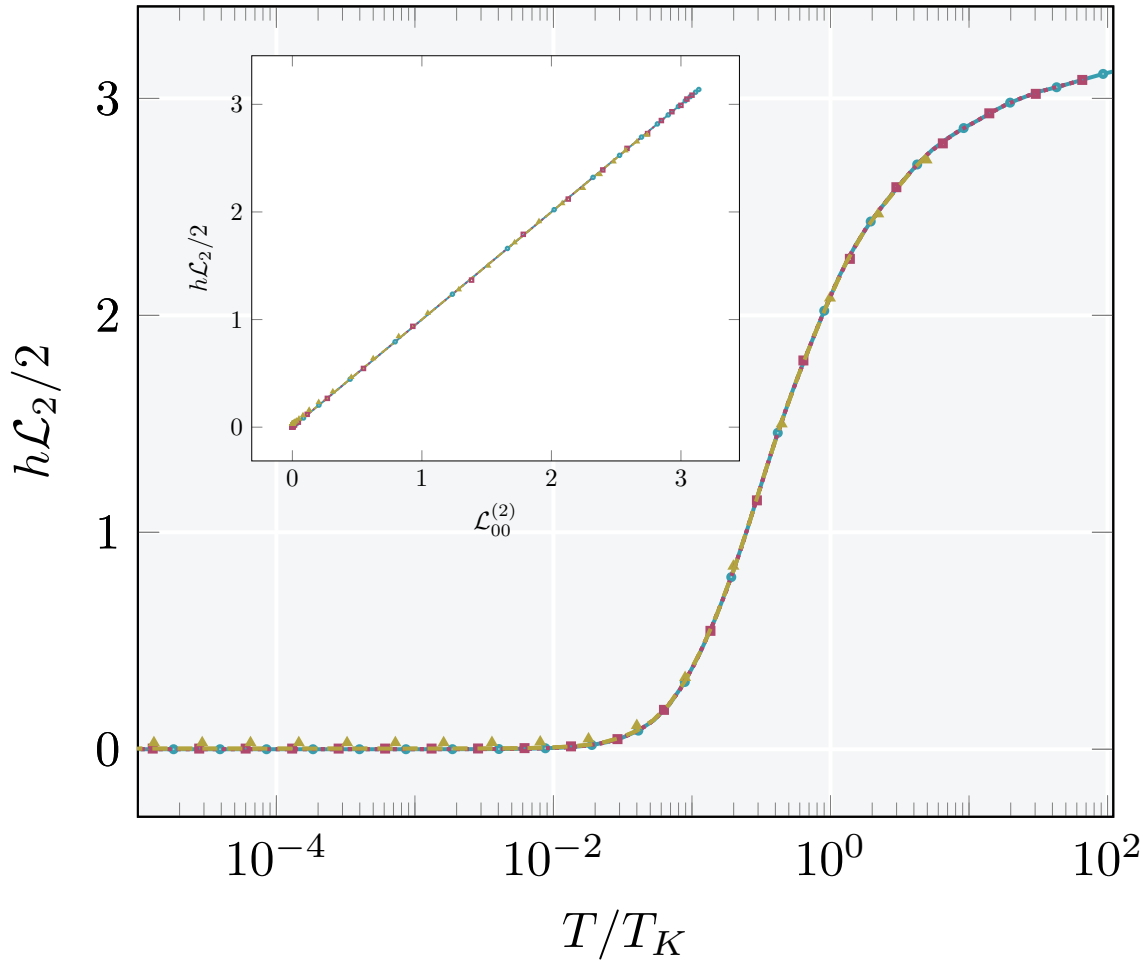Source: By the author.

Figure 19 – Third energetic moment as a function of temperature scaled by T_{K}. It has the greatest contribution to the thermal conductance. The markers, from eNRG runs A-C, are in very good agreement with the solid lines, Eq. 4.33. The inset shows $\mathcal{L}_2(T/T_K)$ as a function of the universal curve $\mathcal{L}_{00}^{(2)}(T/T_K)$. The mapping is also linear.

Source: By the author.

$$\mathcal{L}_0^{\mathrm{FL}} = \frac{2}{h}\cos^2(\delta),$$

$$(5.3)$$

$$\mathcal{L}_2^{\mathrm{FL}} = \frac{2\pi^2}{3h}\cos^2(\delta).$$

Because the energetic moment $\mathcal{L}_1(T/T_{\mathrm{K}})$ vanishes at both fixed points in these regimes, the Wiedmann-Franz law is simply the ratio between the moments $\mathcal{L}_2(T/T_{\mathrm{K}})$ and $\mathcal{L}_0(T/T_{\mathrm{K}})$. From the equations above, it is straightforward to recover the Lorenz number.

Fig. 20 shows the Wiedemann-Franz law for our model, where the black dashed line represents L_0. The eNRG results (scatter points), universality predictions (lines), and the constant L_0 agree well for high and low-temperatures (fixed-points) outside the symmetric

point. The peaks below the Kondo temperature indicate that the Kondo cloud is better at obstructing charge transport than energy flow in this crossover region.

Another characteristic is the height variation of the peaks: it is more pronounced for the magenta squares. We trace this behavior back to Eqs. 4.36 and 4.38. When $\delta = \pi/2$, the differences $\Delta\kappa$ and ΔG between the two fixed points is maximum. On the other hand, there is no difference for $\delta = \pi/4$, and the ratio between the conductances corresponds to the Lorenz number for all temperatures. In the Kondo regime, where universality holds, the phase shifts are always close to $\delta = \pi/2$ and do not reach the temperature independent value associated with $\delta = \pi/4$. Nevertheless, we can interpret the peak height via these arguments so that the magenta squares have a phase shift closer to $\delta = \pi/2$ and have a higher peak.

The inset shows the $V_g = -U/2$ run, which deviates from the Lorenz number at the Frozen Level. Due to particle-hole symmetry, this run has $\delta = \pi/2$, for which both conductances vanish at this fixed point. Their low-temperature expansion determines the ratio between them. The oscillations are a consequence of the discretization and were not completely eliminated by the offset average.

5.4   Efficiency as a thermoelectric device

The device's efficiency as a thermopower generator is determined by a competition between how much energy a Seeback voltage generates and how much energy we lose due to Joule heating and heat conduction. The best devices have a sizeable Seeback coefficient $S(T/T_\mathrm{K})$, a large conductance $G(T/T_\mathrm{K})$ (to reduce Joule heating), and a low thermal conductance $\kappa(T/T_\mathrm{K})$. The dimensionless figure of merit

$$zT \equiv k_\mathrm{B} T \frac{S^2(T)G(T)}{\kappa(T)} \tag{5.4}$$

quantifies this competition. For $zT < 1$, we have small efficiency. The generator's efficiency approaches the ideal Carnot value ν_c for $zT \gg 1$.

Fig. 21 shows the figure of merit as a function of temperature scaled by Kondo temperature for runs A-C of Tab. 4. As before, the lines correspond to the phase shift parametrization, and the points to the eNRG runs. The figure of merit of the symmetric run vanishes, as the thermopower is identically zero. There are peaks below the Kondo temperature for runs B-C, but they are of little practical value. Even at the highest value $zT \approx 0.25$, the figure of merit is small. Hence, the side-coupled device is not a promising thermopower generator.
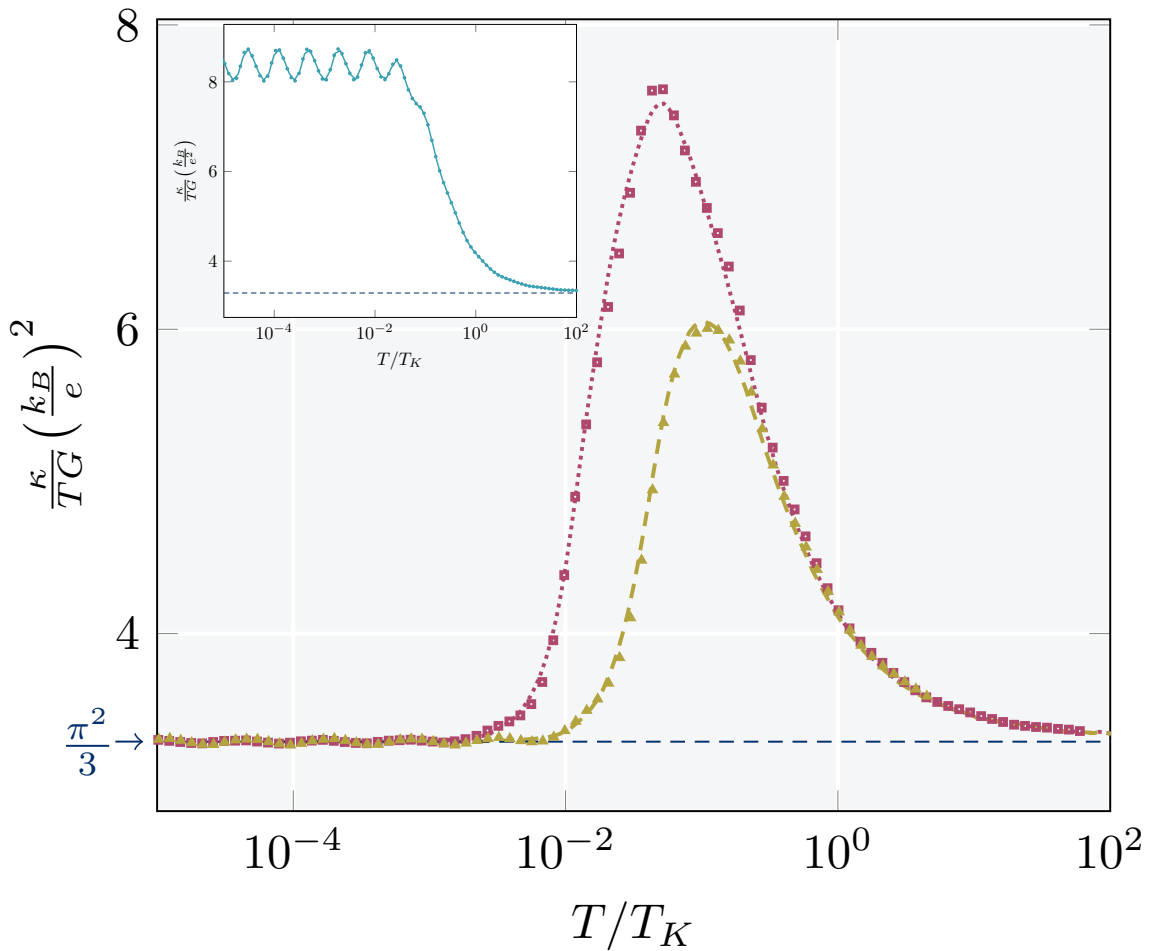
Figure 20 – Wiedemann-Franz ratio as a function of temperature scaled by T_{K}. The symbols and lines correspond to runs A-C in Tab. 4. The high and low temperature behaviours go towards the constant $L_0 = \pi^2/3[k_B/e]$. The inset shows the particle-hole symmetric run, which is markedly different at the Frozen Level fixed-point because both conductance and thermal conductance vanish. The oscillations are an artifact of the conduction-band discretization.
Source: By the author.

5.5 Comparison with experiments

The linear mapping onto universal functions — Eqs. 4.36, 4.37, and 4.38 — benefits interpretation of experimental data. eNRG computes the three functions with minor numerical cost. Then, one must fit merely two free parameters - the phase shift and Kondo temperature - onto measurements in the Kondo regime. The unattainable alternative would be performing numerous eNRG runs looking for a good fit.

This thesis studies the side coupled device, where the coupling between the impurity and conduction band to form the Kondo singlet obstructs transport. We observe the
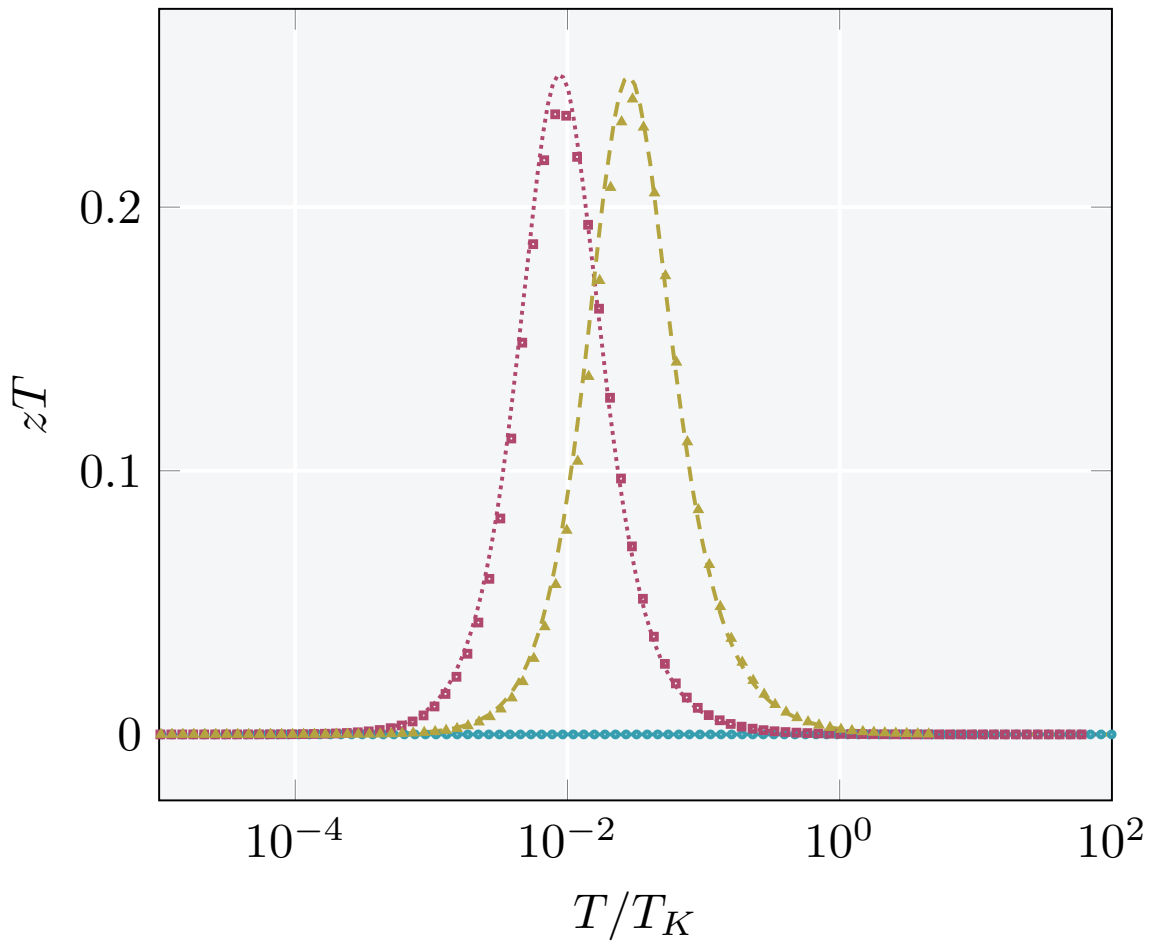
Figure 21 – Dimensionless figure of merit for thermoelectric efficiency as a function of temperature. The symbols and lines correspond to runs A-C in Tab. 4.
Source: By the author.

opposite effect on the single electron transistor, where the impurity links two independent electron gases. Experimental data is available for both devices with caveats. For example, background currents of unknown origin increment the SCD conductances. At the same time, contact asymmetries in the SET make the conductance maxima much lower than the conductance quantum. Fortunately, we do not have to restrict ourselves to data from nanodevices.

The transport obstruction seen on the SCD contains the same physics as the resistance growth in dilute magnetic alloys, which motivated Kondo's original paper. We emphasize this equivalence below by employing the linear mapping to analyze two bulk properties: the conductance and thermopower of rare earth alloys.

5.5.1 Conductance

Under certain conditions, dopants become magnetic impurities. Recent examples are the measurements of $Ce_{1-x}La_xRh_6Ge_4$ resistivity for various dopant concentrations x, performed by Xu *et al.*[2] At high concentrations, $x \to 1$, the Ce ions become exceptions in a regular lattice, i.e., they become impurities. For temperatures below the order of $100K$, crystal field splitting freezes out all but the lowest spin-degenerate level. The Ce ions become magnetic impurities in this context. We now have a spin $1/2$ degree of freedom coupled to the conduction band. To identify the contribution of the magnetic moments to the resistivity, the authors computed the excess resistivity

$$\rho_{\mathrm{mag}} = \frac{\rho_x(T) - \rho_{x=1}(T)}{1 - x}, \qquad (5.5)$$

for the concentrations $x = 0.30, 0.52, 0.66$, and 0.87, represented by the symbols in Fig. 22.

The solid lines in Fig. 22 are predicted by the linear mapping Eq. 4.31, and the first panel shown helps illustrate the fitting procedure. To begin, we must know the universal function $\mathcal{L}^{00}_{(0)}(T/T_{\mathrm{K}})$, which we find with one eNRG run. The conductance, proportional to the inverse resistivity, maps linearly onto the first energetic moment. So, we plot the conductance data versus the universal function for various trial Kondo temperatures, ideally expecting a straight line. Then, we define the optimal choice of T_{K} as the one which maximizes the temperature range where the data agrees with the line. According to the linear mapping equation, both the phase shift and the factor $\mathcal{G}_0$ are now trivially determined, as as they come from the linear fit coefficients. At the Kondo temperature, conductance reaches the value $\mathcal{G}_0/2$, yielding the multiplicative parameter. We then find the phase shift via the slope $-\mathcal{G}_0 \ \cos(2\delta)$.

By applying this same analysis to all dopant concentrations available, we construct Tab. 5, and the second panel of Fig. 22. Here, we left out higher impurity concentrations corresponding to $x = 0 - 0.25$ in Ref. Xu *et al.* We find a poor agreement with the straight lines and slopes corresponding to $\cos \delta > 1$ for these data points. This inconsistency indicates the breakdown of Kondo impurity physics, following the conclusions of Ref. Xu *et al.*

The solid lines for all dopant concentrations disagree with the data points for temperatures $T > 60K$. The discrepancy is also a consequence of the breakdown of Kondo physics. As the temperature increases, crystal field splitting alone can no longer avoid charge fluctuations in the impurities. Consequently, our simple picture of spin $1/2$ degrees of freedom coupled to a conduction band fails, and so does Kondo physics.

Nevertheless, the data points are in excellent agreement with the solid lines for $T < 60K$, except for the higher impurity concentration $x = 0.30$ with $T < 3K$. The worse
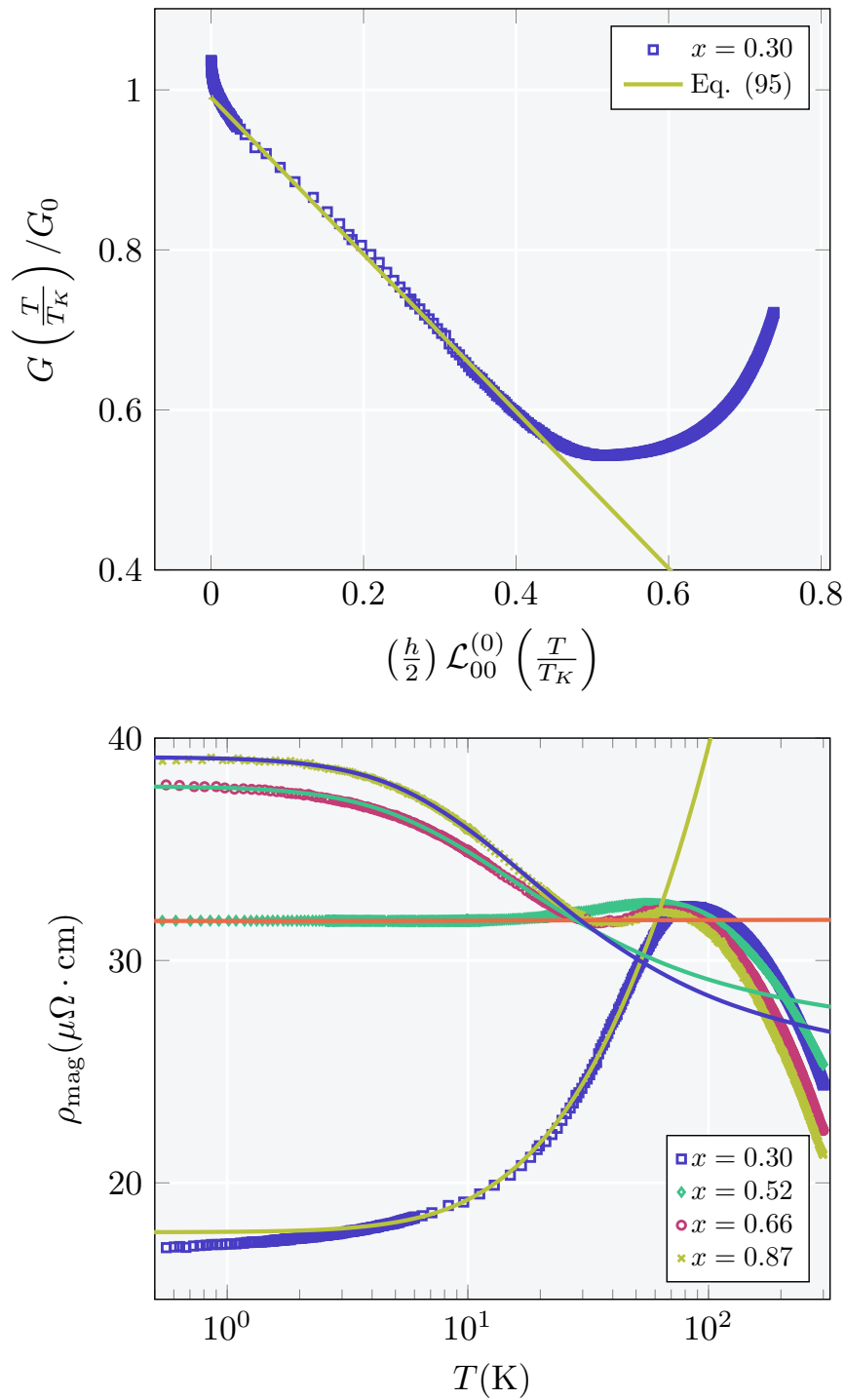
Figure 22 – (a) Fitting procedure, applied to the Ce-ion contribution to the temperature-dependent resistivity of $Ce_{0.7}La_{0.3}Rh_6Ge_2$ reported in Ref. Xu *et al.* [2] The small crosses are the experimental conductivities at the scaled temperatures T/T_K, divided by the adjustable factor $\mathcal{G}_0$ and plotted as functions of the universal function $G_K(T/T_K)$. The straight line is the linear mapping 4.36. (b) Temperature dependence of the Ce-ion contribution to the resistivity of $Ce_{1-x}La_xRh_6Ge_2$ for the indicated dopant concentrations. The symbols show the excess resistivity defined by Eq. 5.5 , and the solid lines, fits of the mapping 4.3 with the parameters in Table 5.
Source: By the author.

Table 5 – Parameters yielding the optimized fits in Fig. 22.

x	$\mathcal{G}_0$(k S/cm)	T_{K}(K)	δ/π
0.87	31.60	31.8	0.280
0.66	31.59	30.0	0.275
0.52	31.46	30.0	0.2504
0.30	31.50	60.5	0.111

Source: By the author.

agreement for higher impurity concentrations is expected. Ce ions, now closer to each other in distance, have a significant RKKY interaction, and can no longer be described by a single impurity model.

5.5.1.1 Thermopower

Unlike the conductance, which involves only one energetic moment, the thermopower is the quotient of two energy moments. Therefore, it is not linearly mapped onto a universal function. We can recover linearity via direct manipulations of Eqs. 4.4, 4.37, and 4.38, which yield

$$h\frac{\mathcal{L}_{01}^{(1)}(T/T_{\mathrm{K}})}{eS(T/T_{\mathrm{K}})} = \frac{\sqrt{2}}{\pi}\left(h\cot(2\delta)\mathcal{L}_{00}^{(0)}(T/T_{\mathrm{K}}) - \cot(\delta)\right). \tag{5.6}$$

Above, we must compute the two energy moments with eNRG runs. Then, if we have experimental values for the thermopower $S(T/T_{\mathrm{K}})$ as a function of temperature, all is left to do is to find the phase shift and the Kondo temperature. We can achieve this goal by a procedure analogous to the one in Sec. 5.5.1.

As no measurements of the thermopower in the SCD have been reported, we again look for an alternative on substitutional alloys with a low concentration of magnetic impurities. Here, we discuss the rare-earth compound $Lu_{0.9}Yb_{0.1}Rh_2Si_2$ and the thermal dependence of its thermopower. Due to crystal field splitting, the ground state multiplet of the Yb ions splits into four doublets. The new ground state lies 210K below the first excitation. Hence, to decrease the contribution of excited states, we focus on temperatures below 75K. Under these circumstances, the Yb impurities become spin 1/2 degrees of freedom coupled to a conduction band, and can therefore be interpreted as a Kondo system.

Fig 23 shows the thermal dependence of the thermopower, where the markers represent the experimental data.[1] The solid lines represent universality predictions given by

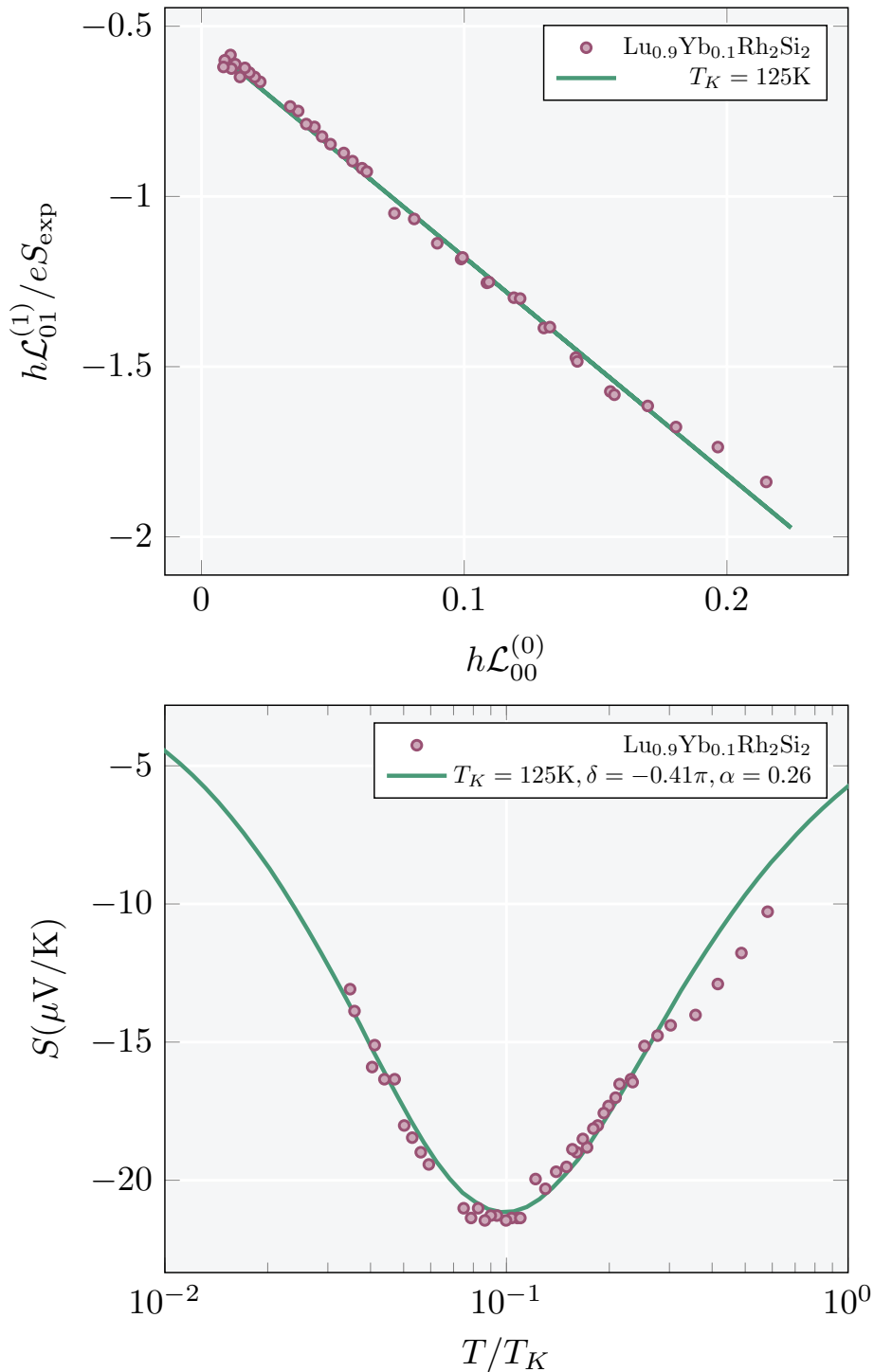$$S(T) = \alpha\frac{2h}{e}\frac{\mathcal{L}_{01}^{(1)}}{h\cot(2\delta)\mathcal{L}_{00}^0 - \cot(\delta)}. \tag{5.7}$$

Figure 23 – Thermopower of the Kondo system $Lu_{0.9}Yb_{0.1}Rh_2Si_2$. The filled circles are measurements reported by Kohler, and the solid lines are optimized fits resulting from Eq. 5.7 with the constants in the legend of panel (b). Panel (a) plots the left-hand side of Eq. 5.6 as a function of $\mathcal{L}_{00}^{(0)}(T/T_K)$ to display the linear regression from which δ and α were obtained.[1] Panel (b) shows the Seebeck coefficient as a function of temperature.

Source: By the author.

Above, the best parameters that describe the data are $T_\mathrm{K} = 125\mathrm{K}$, $\delta = 0.41$ and $\alpha = 0.26$. Once again, we find the Kondo temperature via a bisection procedure and the phase shift and proportionality parameter with the linear fit. The excellent agreement between data and theoretical predictions confirms Köhler's interpretation that the compound's high thermopower originates in the Kondo effect.[1]

One difference between Köhler's work and this thesis deserves attention: the Kondo temperature. Our definition of the Kondo temperature is the point for which the conductance is $\mathcal{G}_0/2$, and it yields 125K for the data shown. Meanwhile, Köhler's definition is that the Kondo temperature corresponds to the thermopower minimum and is 12K. As our previous thermopower calculations show, a ratio of the order $\mathcal{O}(10)$ between these two definitions is natural. Therefore, despite the seeming contradiction, our Kondo temperature value aligns with the experimental work.

6

Summary

At first glance, the most striking feature of the eNRG approach is that its conduction band discretization occurs in real space. In the standard NRG, we define one new operator per logarithmic division of the conduction band. By contrast, in the eNRG, we group bath sites into exponentially growing-sized cells and define one new operator per cell. For this reason, our method is called *exponential* NRG.

The alternative NRG formulation we present has similarities to the standard one. For instance, we also have exponentially decaying hopping coefficients, Eq. 3.40. This feature is a requirement for the iterative diagonalization scheme, which is also present in the eNRG. Moreover, the eNRG and NRG hopping coefficients are asymptotically equivalent if $\lambda^2 = \Lambda$. However, their proportionality breaks down for lower values of n due to the method's distinct dispersion relations. While the eNRG makes no approximations and accounts for the exact tight-binding dispersion $\epsilon_k = -2t \cos(k)$, the NRG typically has a linear dispersion $\epsilon_k = D(k - k_F)$.

Because the typical common ratio value $\lambda = 2$ corresponds to $\Lambda = 4$, an alternative formulation to the z trick was likewise due. In this thesis, it was enough to introduce the offset ζ. This parameter partitions the Hamiltonian into discretized and non-discretized parts and controls the phase of the artificial oscillations introduced by the discretization. By averaging physical properties with $\zeta = 0$ and $\zeta = 1$, we eliminate the unphysical oscillations in temperature. Yet, this critical application is not the only advantage of this parameter. Larger offset values $\zeta \gtrsim 3$ keep larger energy scales in the Hamiltonian. Consequently, it systematically improves the high-temperature/high-energy description. Moreover, it accurately describes energies near the band edges, as shown in Fig. 7.

Beyond its technical advantages, the eNRG method stands out for its simplicity. The common ratio and offset arise naturally and yield simple hopping coefficients. Furthermore, modifications are easier to implement than in its original counterpart.[19] Because the eNRG should be the center of this work, we study the transport properties of a SCD. Combinations of the energy moments $\mathcal{L}_{00}^{(0)}(T/T_{\mathrm{K}})$, $\mathcal{L}_{01}^{(0)}(T/T_{\mathrm{K}})$, and $\mathcal{L}_{00}^{(2)}(T/T_{\mathrm{K}})$

yield conductances, thermal conductances, and thermopowers. In addition, the energy moments are universal functions of temperature divided by the Kondo temperature in the Kondo regime. Figs. 17-19 show the eNRG computations agree very well with the universal mappings Eqs. 4.36-4.38. These analytical mappings act as benchmarks for the eNRG calculations. In addition, they also explain why we have less pronounced deviations from the Wiedemann-Franz law in models with more particle-hole asymmetry (Sec. 5.3); and provide a recipe to find Kondo physics signatures in experimental data (Sec. 5.5).

The eNRG method is more than a mere alternative to NRG. Its core simplicity diminishes the learning barrier to NRG, attracting more young researchers to our field. With this in mind, we made the eNRG python code available. Its better description of high energies and temperatures also shows promising applications of the eNRG as a DMFT impurity solver. Its real space construction is more suitable for the increasingly prominent field of nanodevice experiments. Moreover, a better description of RKKY interactions in two impurity Anderson Models is expected. [19] This is the first work on this new method, and we hope for more to come.

References

1 KÖHLER, U. **Thermoelectric transport in rare-earth compounds**. 2007. Dissertation (Doctor) — Technical University Dresden, Dresden, Germany, 2007.

2 XU, J.-C. *et al.* Ce-site dilution in the ferromagnetic Kondo lattice $CeRh_6Ge_4$. **Chinese Physics Letters**, IOP Publishing, v. 38, n. 8, p. 087101, Sept. 2021.

3 HAAS, W.; BOER, J.; BERG, G. The electrical resistance of gold, copper and lead at low temperatures. **Physica**, v. 1, n. 7, p. 1115–1124, 1934. ISSN 0031-8914.

4 KONDO, J. Resistance minimum in dilute magnetic alloys. **Progress of Theoretical Physics**, v. 32, n. 1, p. 37–49, 1964.

5 WILSON, K. G. The renormalization group: critical phenomena and the Kondo problem. **Reviews of Modern Physics**, American Physical Society, v. 47, p. 773–840, Oct. 1975.

6 BULLA, R.; COSTI, T. A.; PRUSCHKE, T. Numerical renormalization group method for quantum impurity systems. **Reviews of Modern Physics**, American Physical Society, v. 80, p. 395–450, Apr. 2008.

7 PATEL, R.; AGRAWAL, Y.; PAREKH, R. Single-electron transistor: review in perspective of theory, modelling, design and fabrication. **Microsystem Technologies**, Springer, v. 27, n. 5, p. 1863–1875, 2021.

8 BULLA, R. Zero temperature metal-insulator transition in the infinite-dimensional Hubbard model. **Physical Review Letters**, American Physical Society, v. 83, p. 136–139, July 1999.

9 MITCHELL, A. K. *et al.* Generalized Wilson chain for solving multichannel quantum impurity problems. **Physical Review B**, American Physical Society, v. 89, p. 121105, Mar. 2014.

10 STADLER, K. M. *et al.* Interleaved numerical renormalization group as an efficient multiband impurity solver. **Physical Review B**, American Physical Society (APS), v. 93, n. 23, June 2016.

11 BRUOGNOLO, B. *et al.* Open Wilson chains for quantum impurity models: keeping track of all bath modes. **Physical Review B**, American Physical Society, v. 95, p. 121115, Mar. 2017.

12 KRISHNA-MURTHY, H. R.; WILKINS, J. W.; WILSON, K. G. Renormalization-group approach to the Anderson model of dilute magnetic alloys. II. static properties for the asymmetric case. **Physical Review B**, American Physical Society, v. 21, p. 1044–1083, Feb. 1980.

13 SILVA, J. B. *et al.* Particle-hole asymmetry in the two-impurity Kondo model. **Physical Review Letters**, American Physical Society, v. 76, p. 275–278, Jan. 1996.

14 KRISHNA-MURTHY, H. R.; WILKINS, J. W.; WILSON, K. G. Renormalization-group approach to the Anderson model of dilute magnetic alloys. I. static properties for the symmetric case. **Physical Review B**, American Physical Society, v. 21, p. 1003–1043, Feb. 1980.

15 YOSHIDA, M.; SERIDONIO, A. C.; OLIVEIRA, L. N. Universal zero-bias conductance for the single-electron transistor. **Physical Review B**, APS, v. 80, n. 23, p. 235317, 2009.

16 BULLA, R. *et al.* Numerical renormalization group for quantum impurities in a bosonic bath. **Physical Review B**, American Physical Society, v. 71, p. 045122, Jan. 2005.

17 PINTO, J. W. M.; OLIVEIRA, L. N. Recursive computation of matrix elements in the numerical renormalization group. **Computer Physics Communications**, v. 185, n. 4, p. 1299 – 1309, 2014. ISSN 0010-4655.

18 BULLA, R. The numerical renormalization group. *In*: PAVARINE, E.; KOCH, E.; ANDRES, F.; JARRELL, M. (ed.). **Correlated electrons**: from models to material modelling simulation., Germain: Forschungzentrum Julich, 2012. v.2.

19 FERRARI, A. L.; OLIVEIRA, L. N. de. Real-space numerical renormalization group computation of transport properties in side-coupled geometry. **Phys. Rev. B**, American Physical Society, v. 106, p. 075129, Aug 2022. Available at: https://link.aps.org/doi/10.1103/PhysRevB.106.075129.

20 OLIVEIRA, W. C.; OLIVEIRA, L. N. Generalized numerical renormalization-group method to calculate the thermodynamical properties of impurities in metals. **Physical Review B**, American Physical Society, v. 49, p. 11986–11994, May 1994.

21 SERIDONIO, A. C.; YOSHIDA, M.; OLIVEIRA, L. N. Universal zero-bias conductance through a quantum wire side-coupled to a quantum dot. **Physical Review B**, v. 80, p. 235318, 2009.

22 YOSHIDA, M.; OLIVEIRA, L. N. d. Thermoelectric effects in quantum dots. **Physica B**, Elsevier, v. 404, n. 19, p. 3312–3315, 2009.

23 KIM, T.-S.; HERSHFIELD, S. Thermopower of an Aharonov-Bohm interferometer: theoretical studies of quantum dots in the Kondo regime. **Physical Review Letters**, APS, v. 88, n. 13, p. 136601, 2002.

24 FROTA, H. O.; OLIVEIRA, L. N. Photoemission spectroscopy for the spin-degenerate Anderson model. **Physical Review B**, American Physical Society, v. 33, p. 7871–7874, June 1986.

25 LANGRETH, D. C. Friedel sum rule for Anderson's model of localized impurity states. **Physical Review**, American Physical Society, v. 150, p. 516–518, Oct. 1966.

26 SCHRIEFFER, J. R.; WOLFF, P. A. Relation between the Anderson and Kondo hamiltonians. **Physical Review**, American Physical Society, v. 149, n. 2, p. 491–492, 1966.

A

Appendices

Throughout the Appendices, the reader may assume implicit spin sums in every operator, unless stated otherwise.

A.1 Derivation of the simplest eNRG discretization

The problematic term we would like to vanish (from Eq. 3.34) is

$$H_{f\lambda}^{\text{diag}} \equiv -t \sum_{n=1}^{\infty} \sum_{j=1}^{\lambda^n} (\alpha_{n,j}\alpha_{n,j+1}^* + \text{c. c.}) f_n^\dagger f_n. \tag{A.1}$$

The superscript is a reminder that $H_{f\lambda}^{\text{diag}}$ only contains the diagonal terms of $H_{f\lambda}$, which are not present in the non-discretized Hamiltonian.

It is straightforward to see that

$$(\alpha_{n,j}\alpha_{n,j+1}^* + \text{c. c.}) = \text{Re}(\alpha_{n,j}\alpha_{n,j+1}^*), \tag{A.2}$$

which implies the factor inside the parenthesis vanishes if we choose

$$\text{Re}(\alpha_{n,j}\alpha_{n,j+1}^*) = 0. \tag{A.3}$$

Note that due to the complex conjugate operation, which takes $i \to -i$, the imaginary part is not an issue and is always zero. Eq. A.3 is satisfied as long as $\cos(\phi_{n,j} - \phi_{n,j+1}) = 0$, or,

$$\phi_{n,j+1} = \phi_{n,j} + (2p+1)\frac{\pi}{2}, \tag{A.4}$$

where p is an arbitrary integer. Because we have the liberty to choose a phase satisfying Eq. A.4, we pick the most natural option

$$\phi_{n,j} = \phi_n + j\frac{\pi}{2}, \tag{A.5}$$

where ϕ_n denotes a phase that is uniform within each cell, i.e., independent of j.

The j independent phases ϕ_n are yet to be defined. Then, let us consider the second term on the right-hand side of Eq. 3.34:

$$H_{f\lambda}^{\text{off}} = -t \sum_{n=0}^{\infty} (\alpha_{n,\lambda^n}^* \alpha_{n+1,1} \, f_n^\dagger f_{n+1} + \text{H. c.}),$$
(A.6)

where the superscript is a reminder that $H_{f\lambda}^{\text{off}}$ only comprises the off-diagonal terms of $H_{f\lambda}$. Using the recently derived Eq. A.5, we obtain

$$
\begin{aligned}
\phi_{n+1,1} - \phi_{n,\lambda^n} &= \phi_{n+1} - \phi_n + \frac{\pi}{2}(1 - \lambda^n) \\
&= \phi_{n+1} - \phi_n + \frac{\pi}{2}(1 - \mathcal{G}_{n+1} + \mathcal{G}_n),
\end{aligned}
$$
(A.7)

where $\mathcal{G}_n$ is the sum of the sizes of the first n cells. We want the hopping coefficients to be real, positive definite numbers for simplicity and numerical benefit. Then, the choice

$$\phi_n = \frac{\pi}{2}(\mathcal{G}_n + n)$$
(A.8)

achieves this goal. Consequently, Eq. A.8 turns the product of coefficients in the summand on the right-hand side of Eq. A.6 into a negative real number

$$\alpha_{n,\lambda^n}^* \alpha_{n+1,1} = -\left|\alpha_{n,\lambda^n}\right|\left|\alpha_{n+1,1}\right|,$$
(A.9)

and the Hamiltonian Eq. A.6 becomes

$$H_{f\lambda}^{\text{off}} = t \sum_{n=0}^{\infty} (|\alpha_{n,\lambda^n}||\alpha_{n+1,1}| \, f_n^\dagger f_{n+1} + \text{H. c.}).$$
(A.10)

The last step is then selecting the absolute values $|\alpha_{n,j}|$. While they are constrained by their normalization condition, there is no restriction on the j dependence. The simplest and most natural choice, due to the site equivalence of the original model, is a uniform-weight choice. Consequently, the off-diagonal coefficients decay exponentially with n, as expected. This prescription corresponds to

$$\left|\alpha_n\right| = \lambda^{-n/2},$$
(A.11)

and Eq. A.10 becomes

$$H_{f\lambda}^{\text{off}} = t \sum_{n=0}^{\infty} \left(\lambda^{-(n+\frac{1}{2})} \, f_n^\dagger f_{n+1} + \text{H. c.}\right).$$
(A.12)

A.2   Analogue of the z-trick

In standard NRG, the z trick introduces a second parameter. This real number, $z \in [0.5, 1.5]$ changes the intervals of the logarithmic discretization to

$$\{1, \Lambda^{-1}, \Lambda^{-2}, ...\} \to \{1, \Lambda^{-z}, \Lambda^{-1-z}, ...\}.$$
(A.13)

Consequently, the hopping coefficients become

$$t_n^z = \frac{1 + \Lambda^{-1}}{2} \Lambda^{1-z-\frac{n}{2}}. \tag{A.14}$$

Averaging results over z eliminates the unwanted oscillations. To be precise, it can be shown that the amplitude of deviations in equilibrium transport properties is proportional to

$$\bar{f}_{\Lambda,z} = \cos(\theta_1 + 2\pi(z-1)) \exp\left(-\frac{\pi^2}{\log(\Lambda)}\right), \tag{A.15}$$

where θ_1 is the phase of the $z = 1$ oscillation [20]. Due to the trigonometrical pre-factor, $\bar{f}_{\Lambda,z=0.5} = -\bar{f}_{\Lambda,z=1}$, so averaging transport properties over these two z values eliminates the oscillatory behavior.

To construct the analogous extension for eNRG, we must define a new parameter w, denoted *seed width*. Now, for offset $\zeta = 0$, instead of λ^n sites, the n-th cell contains $w\lambda^{n-1}$ sites, for $n > 0$. The distinction for $n = 0$ is because the first cell, coupled to the impurity, always has one site. The cell broadening then changes the coefficients $\alpha_{n,j}$, which become

$$\left|\alpha_{n,j}\right| = \begin{cases} 1 & (n = 0) \\ (w\lambda^{n-1})^{-1/2} & (n \geq 1) \end{cases}. \tag{A.16}$$

Consequently, the hopping coefficients of the discretized Hamiltonian also change, and become

$$t_n^w = \begin{cases} t(\frac{w}{2})^{-1/2} & (n = 0) \\ t(w\lambda^{n-\frac{1}{2}})^{-1} & (n \geq 1) \end{cases}. \tag{A.17}$$

We relate the parameters z and w by comparing Eqs. A.14 and A.17, that is,

$$\frac{t_n^z}{(1 + \Lambda^{-1})/2} \equiv \frac{t_n^w}{\sqrt{2}} \xrightarrow{\Lambda \to \lambda^2} z \equiv 1 + \frac{\log(\omega)}{2\log(\lambda)}. \tag{A.18}$$

Finally, because $w = \lambda$ and $w = 1$ correspond exactly to the offsets $\zeta = 0$ and $\zeta = 1$, we find the relation

$$\begin{aligned} \zeta = 0 &\iff z = 1.5 \\ \zeta = 1 &\iff z = 1 \end{aligned} \tag{A.19}$$

.

Hence, an average between these offsets indeed eliminates the oscillations.

A.3 Diagonalization of the fixed point Hamiltonians

The Frozen Level and Local Moment Hamiltonians take the form

$$H^* = \sum_k \epsilon_k a_k^\dagger a_k + W^* f_0^\dagger f_0 \tag{A.20}$$

As they are quadratic, it is possible to write them as

$$H_* = \sum_\ell \varepsilon_\ell g_\ell^\dagger g_\ell, \tag{A.21}$$

where

$$g_\ell = \sum_q \alpha_{\ell q} a_q. \tag{A.22}$$

. Then, it follows from the commutator $[g_\ell, H^*]$ that

$$\alpha_{\ell q} = \frac{1}{\varepsilon_\ell - \epsilon_q} \frac{W^*}{N} \sum_k \alpha_{\ell k} \tag{A.23}$$

which becomes by summing in q,

$$1 = \frac{W^*}{N} \sum_q \frac{1}{\varepsilon_\ell - \epsilon_q}. \tag{A.24}$$

.

We compute the sum in on the right hand side of Eq. $A.24$ with a Sommerfeld-Watson transformation. The starting point is the definition of the energies ε_ℓ and ϵ_q in the eNRG framework. If $\ell, q \in \mathbb{Z}$,

$$\epsilon_q = \begin{cases} \lambda^{-2q} & q > 0 \\ -\lambda^{2q} & q < 0 \end{cases}, \tag{A.25}$$

and

$$\varepsilon_\ell = \begin{cases} \epsilon_\ell\, \lambda^{2\delta/\pi} & \ell > 0 \\ \epsilon_\ell\, \lambda^{-2\delta/\pi} & \ell < 0 \end{cases}, \tag{A.26}$$

where δ is a $\mod(\pi)$ parameter describing the eigenvalue phase-shift.

Subsequently, we define the function

$$F(z) = \frac{\pi \cot(\pi z)}{\varepsilon_\ell - \epsilon(z)}, \tag{A.27}$$

whose poles are the integer numbers and z such that $\epsilon(z) = \varepsilon_\ell$. The poles and the integration path are shown in Fig 24. By applying the residue theorem to $F(z)$, we obtain

$$\sum_q \frac{1}{\varepsilon_\ell - \epsilon_q} = -\frac{\pi}{2\ln(\lambda)\varepsilon_\ell} \cot \delta + \frac{1}{2\pi i} \int_C dz \frac{\pi \cot(\pi z)}{\varepsilon_\ell - \epsilon(z)}. \tag{A.28}$$
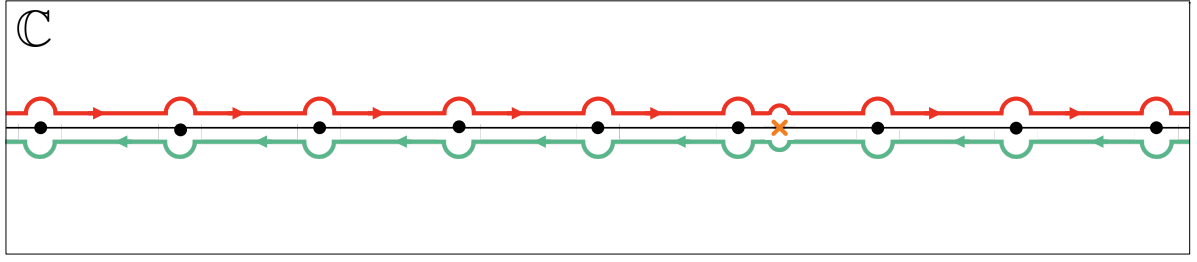
Figure 24 – Integration path for the Sommerfeld-Watson transformation.
Source: By the author.

The z dependence of the integrand on the right hand size of Eq. $A.28$ poses a problem in analytically deforming the paths to infinite pure imaginary numbers, as

$$\lim_{z\to\pm i\infty} \cot(\pi z) = \mp i. \tag{A.29}$$

To avoid this issue, we define the functions

$$h_{\pm}(z) = \cot(\pi z) \pm i, \tag{A.30}$$

so that

$$\lim_{z\to\pm i\infty} h_{\pm}(z) = 0. \tag{A.31}$$

Then, we rewrite the integral as

$$\int_C dz \frac{\pi \cot(\pi z)}{\varepsilon_\ell - \epsilon(z)} = \int_{C_+} \frac{\pi(h_+(z) - i)}{\varepsilon_\ell - \epsilon(z)} + \int_{C_-} \frac{\pi(h_-(z) + i)}{\varepsilon_\ell - \epsilon(z)}, \tag{A.32}$$

where C_+ and C_- are the upper and lower paths in Fig. 24. As all poles lie on the real axis, we deform these paths to infinity and minus infinity, respectively. By construction, the integrals containing the functions $h_{\pm}(z)$ vanish. The Sommerfeld-Watson transformation yields

$$\sum_q \frac{1}{\varepsilon_\ell - \epsilon_q} = -\pi \rho \cot \delta + \fint_{-D}^{D} \frac{d\varepsilon}{|\varepsilon|} \frac{1}{\varepsilon_\ell - \varepsilon}, \tag{A.33}$$

where

$$\rho = \frac{1}{2\ln(\lambda)\varepsilon_\ell}. \tag{A.34}$$

At low energies, the integral contributes with a term of order $\mathcal{O}(\epsilon/D)$, which we neglect. Hence, the uniform phase shifts are

$$\tan(\delta) = -\frac{\pi \rho W^*}{N}. \tag{A.35}$$

After determining the phase shifts of the energy spectrum, the next step is to find the coefficients which determine the eigenstates, $\alpha_{\ell q}$. The square of Eq. $A.58$, with a subsequent sum in q yields

$$1 = \left(\sum_k \alpha_{\ell k} \frac{W^*}{N}\right) \sum_q \frac{1}{(\varepsilon_\ell - \epsilon_q)^2}. \tag{A.36}$$

Then, by differentiating Eq. $A.33$ with respect to δ_ℓ, we obtain for the energy sum above

$$\sum_q \frac{1}{(\varepsilon_\ell - \epsilon_q)^2} = \left(\frac{\pi\rho}{\sin(\delta_\ell)}\right)^2, \tag{A.37}$$

and hence

$$\frac{W^*}{N} \sum_k \alpha_{\ell k} = -\frac{\sin(\delta_\ell)}{\pi\rho}. \tag{A.38}$$

This result, together with Eq. $A.58$, allows us to write $\alpha_{\ell q}$, i.e.,

$$\alpha_{\ell q} = -\frac{1}{\varepsilon_\ell - \epsilon_q}\frac{\sin(\delta_\ell)}{\pi\rho}. \tag{A.39}$$

A.4   Decomposing non-universal matrix elements

The goal of this appendix is to show how matrix elements of the operators $\langle m| a_0 |n\rangle$ can be decomposed into a linear combination of the universal matrix elements $\langle m| \phi_0 |n\rangle$ and $\langle m| \phi_1 |n\rangle$. The starting point is the assumption that the eigenvalues E_m and E_n are much smaller than the conduction bandwidth, that is,

$$|\mathcal{E}_{mn}| \ll 1, \tag{A.40}$$

where $\mathcal{E}_{mn} \equiv (E_m - E_n)/D$.

We define the universal quantities

$$M_{mn}^{(p)} \equiv \frac{1}{\sqrt{N}} \sum_\ell \left(\frac{\varepsilon_\ell}{D}\right)^p \langle m| g_\ell |n\rangle, \tag{A.41}$$

which, in the Kondo regime, can be evaluated in the symmetric point with no loss of generality. In that case, we work with the particle-hole symmetric Hamiltonian and write the commutator

$$[g_\ell, H_A^S] = \epsilon_\ell + \frac{V}{\sqrt{N}}c_d. \tag{A.42}$$

In order to write the above commutator in terms of the quantities in Eq. $A.41$, we multiply the whole equation by $(\varepsilon_\ell/D)^{p-1}$ and sum in ℓ. The term that can not be rewritten in this manner is transformed into an integral. The resulting recursive equations are

$$M_{mn}^{(p)} = \begin{cases} -\mathcal{E}_{mn}M_{mn}^{(p-1)} - \frac{2V\rho}{N}\frac{\langle m|c_d|n\rangle}{p} & p = 1, 3, ... \\ -\mathcal{E}_{mn}M_{mn}^{(p-1)} & p = 2, 4, ... \end{cases} \tag{A.43}$$

The recursive equations can be readily solved by induction, and their solutions are

$$M_{mn}^{(p)} = -\mathcal{E}_{mn}^{(p)}M_{mn}^{(0)} - \frac{2V\rho}{N}\sum_{r=1}^{p}{}' \frac{(\mathcal{E}_{mn})^{r-1}}{p-r+1}, \tag{A.44}$$

when $p = 1, 3, ...$ and

$$M_{mn}^{(p)} = \mathcal{E}_{mn}^{(p)} M_{mn}^{(0)} + \frac{2V\rho}{N} \sum_{r=1}^{p-1} {}' \frac{(\mathcal{E}_{mn})^r}{p-r}, \tag{A.45}$$

when $p = 2, 4, ...$ In both cases, the primed sum runs over odd integers.

As a consequence of Eq. $A.40$, it is a good approximation to only take into account terms of $\mathcal{O}(\mathcal{E}_{mn}^0)$. Hence, the only non-vanishing term is the one with $r = 1$ in Eq. $A.44$, and we obtain

$$M_{mn}^{(p)} = \begin{cases} \frac{\sqrt{N}}{3} \frac{\langle m|\phi_1|n\rangle}{p} & p = 1, 3, ... \\ 0 & p = 2, 4, ... \end{cases} \tag{A.46}$$

The orthonormal basis of conduction states

$$\phi_\ell \equiv \sqrt{\frac{2\ell+1}{N}} \sum_p P_\ell(\epsilon_p) g_p \quad \ell = 0, 1, ..., \tag{A.47}$$

is useful, where $P_\ell(\epsilon_p)$ are Legendre Polynomials. The matrix elements $\langle n| \phi_\ell |n\rangle$ are linear combinations of the universal quantities $M_{mn}^{(p)}$, Eq. $A.41$. Hence, it follows from $A.46$ that

$$\langle m| \phi_\ell |n\rangle \propto \begin{cases} \langle m| \phi_1 |n\rangle & p = 1, 3, ... \\ 0 & p = 2, 4, ... \end{cases} \tag{A.48}$$

As a consequence, by writing any operator $\{f_i\}$ as a linear combination of operators $\{\phi_\ell\}$, we obtain

$$\langle m| f_i |m\rangle = \sum_{j=0,1} \alpha_{i,j} \langle m| \phi_j |n\rangle, \tag{A.49}$$

where $\alpha_{i,j}$ are model-parameter dependent constants.

A.5 Relating the spectral densities

The starting point to relate the spectral densities $\rho_0(\epsilon, T)$ and $\rho_1(\epsilon, T)$ is the closed form of the conduction-electron retarded Green's function for the symmetric Anderson Hamiltonian, i.e.,

$$\mathbb{G}_{kk'}^S(\epsilon) = \mathbb{G}_k^0(\epsilon)\delta_{kk'} + \frac{V^2}{N}\mathbb{G}_k^0(\epsilon)\mathbb{G}_d^S(\epsilon)\mathbb{G}_{k'}^0(\epsilon), \tag{A.50}$$

where

$$\mathbb{G}_k^0 = \frac{1}{\epsilon - \epsilon_k + i\eta} \tag{A.51}$$

is the free conduction-electron retarded Green's function and $\mathbb{G}_d^S(\epsilon)$ is the dot level retarded Green's function for the symmetric Hamiltonian. Because the operators ϕ_0 and ϕ_1 are linear combinations of the operators g_k, we compute the spectral densities by the sums

$$\rho_0(\epsilon, T) = -\frac{1}{\pi N}\Im \sum_{kk'} \mathbb{G}_{kk'}^S, \tag{A.52}$$

and

$$\rho_1(\epsilon, T) = -\frac{3}{\pi N D^2} \Im \sum_{kk'} \epsilon_k \epsilon_{k'} \mathbb{G}^S_{kk'}. \tag{A.53}$$

The free conduction-electron Green's function has a implicit limit $\eta \to 0^+$. As a consequence, it is possible to rewrite it as

$$\mathbb{G}^0_k = \frac{1}{\epsilon - \epsilon_k} - i\pi\delta(\epsilon - \epsilon_k). \tag{A.54}$$

To further simplify the problem, we notice that in the Kondo regime Eq. 2.10, excitation energies are much smaller than the conduction band half-width D. Hence, for parameters in the Kondo regime, it is sufficient to consider $\epsilon \ll D$, and to neglect terms of the order $\mathcal{O}(\epsilon/D)$. Then, by transforming the sums $A.52$ and $A.53$ into integrals, we obtain

$$\rho_0(\epsilon, T) = \frac{\rho}{N} - \left(\frac{\pi\rho V}{N}\right)^2 \rho^S_d(\epsilon, T), \tag{A.55}$$

and

$$\rho_1(\epsilon, T) = 12\left(\frac{\rho V}{N}\right)^2 \rho^S_d(\epsilon, T). \tag{A.56}$$

Accordingly, the relationship between the spectral functions is

$$\rho_0(\epsilon, T) = \rho - \frac{\pi^2}{12}\rho_1(\epsilon, T). \tag{A.57}$$

A.6 Fixed point spectral densities

The fixed point spectral densities are essential to determine the constants α_0 and α_1 on Eq. 4.24. The first step in its computation is evaluating the commutator $[H_A, a^\dagger_q]$, where $a^\dagger_q$ creates one particle with momentum q. Evaluated in the fixed point eigenstates $|m\rangle$ and $|n\rangle$, this commutator yields

$$\langle m| a^\dagger_q |n\rangle = \frac{V}{\sqrt{N}} \frac{\langle m| d^\dagger |n\rangle}{E_m - E_m - \epsilon_q}. \tag{A.58}$$

The basis $\{g_\ell\}$, in which the fixed point Hamiltonian is diagonal, relates to the basis $\{a_q, d\}$ via the orthonormal transformation

$$g_\ell = \gamma_{\ell 0}\, d + \sum_q \gamma_{\ell q}\, a_q. \tag{A.59}$$

A substitution on Eq. $A.58$ results in

$$\sum_\ell \left(\gamma_{\ell q} - \frac{V}{\sqrt{N}} \frac{\gamma_{\ell 0}}{E_m - E_n - \epsilon_q}\right) \langle m| g^\dagger_\ell |n\rangle = 0 \tag{A.60}$$

As long as $|m\rangle = g_\ell^\dagger |n\rangle$, the equation above, together with the normalization condition for g_ℓ, uniquely defines the coefficient $\gamma_{\ell 0}$. If the matrix element is not zero, the term inside the rounded brackets must be zero. Then, we sum the equation for $\gamma_{\ell 0}$ in q and use Eq. A.37 to write

$$\gamma_{\ell 0}^2 = \frac{1}{1 + \frac{N\sin^2(\delta^*)}{(V\pi\rho)^2}}. \tag{A.61}$$

We are interested in the low energy result, where $\varepsilon_\ell \ll D$. As $\rho \propto \varepsilon_\ell^{-1}$, it suffices to work with the approximation

$$\gamma_{\ell 0}^2 = \frac{\sin^2(\delta^*)}{N(V\pi\rho)^2}, \tag{A.62}$$

Moreover, we write the operator d in the $\{g_\ell\}$ basis by inverting Eq. $A.59$. As a consequence, Eq. $A.62$ becomes

$$|\langle m| d^\dagger |n\rangle|^2 = \frac{N\sin^2(\delta^*)}{(V\pi\rho)^2}, \tag{A.63}$$

for $|m\rangle = g_\ell^\dagger |n\rangle$.

The spectral density $\rho_0(\epsilon, T)$ depends on matrix elements of the operator f_0. The computation of these matrix elements becomes a simple matter with Eqs. $A.58$ and $A.63$. Therefore, we multiply Eq. $A.58$ by its complex conjugate, sum in q and substitute Eq. $A.63$ to write

$$|\langle m| f_0^\dagger |n\rangle|^2 = \frac{\cos^2(\delta^*)}{N}. \tag{A.64}$$

Thus, the spectral density with $i = 0$, Eq. 4.22, is

$$\rho_0(\epsilon, T) = \rho \; \cos^2(\delta^*), \tag{A.65}$$

on the fixed points. In particular, we denote the Frozen Level phase shift by $\delta^* = \delta$, and the Local Moment phase shift by $\delta^* = \delta - \pi/2$. Hence, the final forms of the fixed point spectral densities are

$$\rho_0^{FL}(\epsilon, T) = \rho \; \cos^2(\delta), \tag{A.66}$$

and

$$\rho_0^{LM}(\epsilon, T) = \rho \; \sin^2(\delta). \tag{A.67}$$

The equations above enable us to compute the fixed points energetic moments. The knowledge of one fixed point energetic moment is sufficient to determine the constants α_0 and α_1. We chose to work with $n = 0$ in Eq. 4.1. Its fixed points values are

$$\mathcal{L}_0^{FL}(\epsilon, T) = \frac{2\rho}{h} \cos^2(\delta), \tag{A.68}$$

and

$$\mathcal{L}_0^{LM} = \frac{2\rho}{h} \sin^2(\delta). \tag{A.69}$$